Received: 4 March 2022 | Revised: 18 August 2022 | Accepted: 21 August 2022

DOI: 10.1002/fld.5143

RESEARCH ARTICLE

WILEY

A semi-implicit finite volume scheme for a simplified hydrostatic model for fluid-structure interaction

Cristian Brutto | **Michael Dumbser**

Laboratory of Applied Mathematics, University of Trento, Trento, Italy

Correspondence
Michael Dumbser, Laboratory of Applied Mathematics, University of Trento,
Via Mesiano 77, 38123 Trento (TN), Italy.
Email: michael.dumbser@unitn.it

Funding information
Bundesanstalt für Wasserbau; Istituto Nazionale di Alta Matematica "Francesco Severi"; Ministero dell'Istruzione, dell'Università e della Ricerca

Abstract

Simulating fluid-structure interaction problems usually requires a considerable computational effort. In this article, a novel semi-implicit finite volume scheme is developed for the coupled solution of free surface shallow water flow and the movement of one or more floating rigid structures. The model is well-suited for geophysical flows, as it is based on the hydrostatic pressure assumption and the shallow water equations. The coupling is achieved via a nonlinear volume function in the mass conservation equation that depends on the coordinates of the floating structures. Furthermore, the nonlinear volume function allows for the simultaneous existence of wet, dry and pressurized cells in the computational domain. The resulting mildly nonlinear pressure system is solved using a nested Newton method. The accuracy of the volume computation is improved by using a subgrid, and time accuracy is increased via the application of the theta method. Additionally, mass is always conserved to machine precision. At each time step, the volume function is updated in each cell according to the position of the floating objects, whose dynamics is computed by solving a set of ordinary differential equations for their six degrees of freedom. The simulated moving objects may for example represent ships, and the forces considered here are simply gravity and the hydrostatic pressure on the hull. For a set of test cases, the model has been applied and compared with available exact solutions to verify the correctness and accuracy of the proposed algorithm. The model is able to treat fluid-structure interaction in the context of hydrostatic geophysical free surface flows in an efficient and flexible way, and the employed nested Newton method rapidly converges to a solution. The proposed algorithm may be useful for hydraulic engineering, such as for the simulation of ships moving in inland waterways and coastal regions.

KEYWORDS

fluid-structure interaction, pressurized flow, rigid body motion, semi-implicit finite volume scheme, subgrid, wetting and drying

1 INTRODUCTION

Fluid-structure interaction problems have numerous applications in science and engineering, both for the effects of the fluid on the solid and vice versa. The range of solutions available is broad, and usually the choice of the numerical implementation is a trade-off between accuracy, speed of computation, and complexity. We mention here a few examples. Bradford[1] proposed a model in which the structure is the void resulting from the vertical subdivision of the domain in two regions of water, and each region is discretized by a σ-coordinate transformation of the grid. In the context of potential-flow theory, Shao et al.[2] include a floating body using a higher-order boundary element method, while Tong et al.[3] implement an immersed boundary method combined with a harmonic polynomial cell method. Ferrari and Dumbser[4] developed a semi-implicit finite volume scheme for the free-surface equations written in a conservative form that treats the nonhydrostatic pressure exerted against a fixed rigid body; in particular they use the diffuse interface approach, in which for each cell along the vertical the volume is limited and subdivided in the liquid, solid and void phases, while the pressure is unbounded. Similar diffuse interface models in the context of weakly compressible flows have been forwarded, for example, in References 5 and 6 and references therein.

Numerical methods for pressurized flows are often derived for stormwater systems, in which the flow transits from a free-surface condition to a pressurized regime, where it is then called mixed flow. The numerical solutions for this type of problem differ in how many sets of equations are adopted, either one working in both free-surface and pressurized conditions, or two. Some examples of these schemes are the Preissmann slot technique[7,8] and the two-component pressure approach;[9] for more details, see the review by Bousso et al.[10]

One very important element to consider is if dispersion effects are required, or not, and if the region near the floating body needs to be treated differently from the rest of the domain. Bosi et al.[11] show that when there are no rotational degrees of freedom, high-order dispersive terms become negligible and therefore a simple hydrostatic shallow water model is appropriate in the near body region. Work in this direction has been also done by Lannes[12] and Godlewski et al.,[13,14] who coupled a shallow water model with the motion of a rigid body; in the case examined by Bocchi et al.[15] the structure is fixed. However, the waves generated by the fluid-structure interaction can travel far from the body and may also be dispersive in nature; consider, for example, precursor solitons or the Kelvin wake.[16] In these cases, it is advisable to introduce dispersion effects outside the near-body region to take into account nonhydrostatic effects as well. This can be done either by employing a multilayer nonhydrostatic model, see for example, References 17 and 18, or Boussinesq-type models.[19-21] An example of the former model can be found in the work of Rijnsdorp and Zijlema:[22] in their extension of the nonhydrostatic SWASH model,[23] they integrate a body with a fixed position into the domain. Examples of application of the Boussinesq-type approximation can be found in the works of Bingham,[24] Karambas and Loukogeorgaki[25] and Beck and Lannes.[26] A high order discontinuous Galerkin finite element method for the simulation of the coupling of dispersive water waves with structures can be found in Reference 27. For recent and very efficient hyperbolic reformulations of nonlinear dispersive shallow water flows, see for example, References 28-32 and references therein. The introduction of dispersion effects is outside the scope of this article, meaning that the nonlinear shallow water equations are applied in the entire domain; nonetheless, given their importance for predicting the wave dynamics, future developments of the model presented in this article will include also nonhydrostatic effects.

The method used in this article for the pressurized part of the flow was developed by Casulli and Stelling.[33] The main idea is to write the water depth in the mass conservation equation as a piecewise linear function limited from both below and above. The limit below could represent the bathymetry of a river bed or the bottom of a pipe, while the limit on top may be a floating structure or the roof of a pipe. With this boundary from above, when the flow is pressurized, the wet cross section is limited while the pressure can increase. Other works that laid the foundation for this article are those of Casulli and Walters,[34] and Casulli and Stelling[35] on staggered semi-implicit finite volume/finite difference schemes for free surface flows. The main contribution of this article is the extension of these methods to work with floating objects. For recent results on alternative staggered semi-implicit finite volume and finite element schemes for the shallow water and Navier-Stokes equations, the reader is referred to References 36-40. In the new method proposed in this article the hydrodynamics is solved in terms of conservative variables, in order to deal also with bores and hydraulic jumps. We assume a hydrostatic-pressure distribution in water, and in this context we develop a new and efficient semi-implicit finite volume model for fluid-structure interaction problems (SIFSI). The model originates from the shallow water equations written in a conservative form, and the water flow is coupled with the equations of motion of a rigid floating body. The resulting sparse mildly nonlinear system for free-surface and pressurized flows is linearized by the nested Newton method of Casulli et al.,[41-44] and it is then solved by a matrix-free conjugate gradient method since the resulting pressure systems are symmetric and positive definite. Mass is exactly conserved at each time step, even when cells in the computational domain are undergoing wetting and drying. The floating body, which we will refer to also as the "ship", "boat", or "vessel", has six degrees of freedom, three for its translational and three for its rotational degrees of freedom. The forces acting on it are only those resulting from gravity and from the hydrostatic pressure pushing on its external surface. As a result, the water waves affect the movement of the ship, but the equation coupling works both ways, meaning that the ship changes the water depth in the space below it, generating radiated waves as it moves. The computational grid is staggered and nonconforming. A subgrid[45] efficiently integrates the details of the bathymetry and of the floating body, improving the accuracy of volume computations at a reasonable computational cost. In addition, we make use of the theta method to reduce numerical dissipation and thus preserve wave height.

These types of models generate results rapidly without sacrificing accuracy, where it matters. They could be of interest to the shipbuilding industry, because they allow to observe the response of the floating body in different conditions, such as in open and confined shallow waters.[46] They allow to perform simulations for multiple hull types and to study their interaction with the boundaries.[47] When they are applied to predict the response in working conditions and with complex bathymetries, such as during maneuvers in inland waterways or harbors, they can assess the generation of waves and the interplay with other bodies and structures. However, we would like to clearly emphasize that the hydrostatic pressure assumption made in this article may be very restrictive for general fluid-structure applications and for a wider range of wavenumbers. Future work will therefore be dedicated to extend the model presented in this article to more general nonhydrostatic flows, which are, however, out of scope of the present article. In addition, another possible application of these models is the prediction of the interaction between waves and wave energy converters (WEC), and their consequent motion.[48]

The article is organized as follows: in Section 2, the equations are written for a one-dimensional domain, and the components of the method are added progressively in order to ease comprehension and to offer a clear guideline for readers who want to implement this method. Then, the scheme is generalized by adding the vertical component, and ultimately the transversal component, obtaining a three-dimensional hydrostatic fluid-structure-interaction (FSI) model. In Section 3, the model is tested in different scenarios and the obtained numerical results are compared to available exact solutions to verify the water flow and the movement of the floating body. In Section 4, we summarize and comment on the characteristics of the method, and we outline some possible improvements, which will be the subject of future work.

2 | NUMERICAL METHOD

2.1 | Staggered Cartesian mesh

The method presented in this article is a semi-implicit finite volume scheme on a *staggered grid*: in the most general 3D case the physical domain $\Omega \in \mathbb{R}^3$ is discretized by a set of cells $\Omega_{i,j,k} = \left[x_{i-\frac{1}{2}}, x_{i+\frac{1}{2}}\right] \times \left[y_{j-\frac{1}{2}}, y_{j+\frac{1}{2}}\right] \times \left[z_{j-\frac{1}{2}}, z_{j+\frac{1}{2}}\right]$ forming a Cartesian grid of mesh spacings $\Delta x_i = x_{i+\frac{1}{2}} - x_{i-\frac{1}{2}}$, $\Delta y_j = y_{j+\frac{1}{2}} - y_{j-\frac{1}{2}}$, $\Delta z_k = z_{k+\frac{1}{2}} - z_{k-\frac{1}{2}}$ and barycenter coordinates $x_i = \frac{1}{2}\left(x_{i-\frac{1}{2}} + x_{i+\frac{1}{2}}\right)$, $y_j = \frac{1}{2}\left(y_{j-\frac{1}{2}} + y_{j+\frac{1}{2}}\right)$, $z_k = \frac{1}{2}\left(z_{k-\frac{1}{2}} + z_{k+\frac{1}{2}}\right)$, respectively. Throughout this article the axes x, y, z and the indices for the variables i, j, k will follow the orientations depicted in Figure 1, where north, south, east, west have nothing to do with the actual orientation in the physical space, but they are just labels for the faces to refer to them unequivocally. For the 1D model we consider a domain formed by $I_{\max}$ cells along the x axis, for the 2D_{xz} model we have an additional subdivision in up to $K_{\max}$ cells along the vertical axis z, and for the 3D we add the horizontal subdivision in $J_{\max}$ cells along the y axis. In each cell some variables are defined in the center and they represent the average value $a_{i,j,k}$ of a generic quantity $a(x, y, z)$

$$a_{i,j,k} = \frac{1}{|\Omega_{i,j,k}|} \int_{\Omega_{i,j,k}} a(x, y, z)\, dxdydz, \qquad |\Omega_{i,j,k}| = \int_{\Omega_{i,j,k}} dxdydz,$$

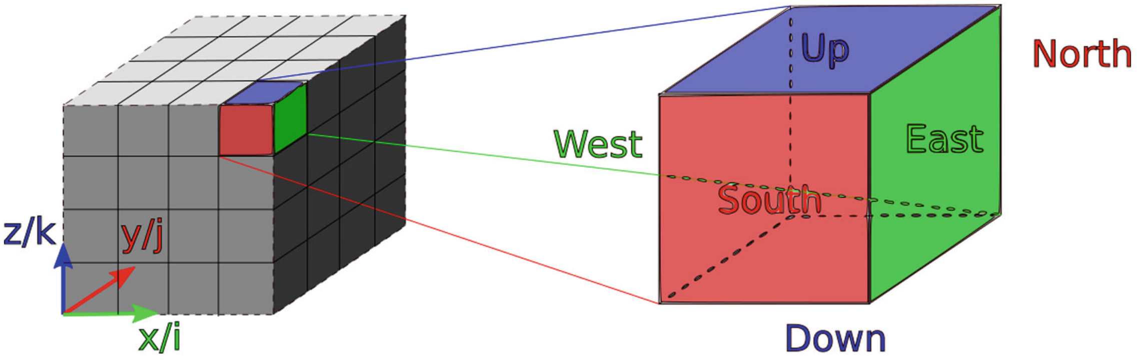

FIGURE 1 Representation of the 3D computational domain and faces orientation [Colour figure can be viewed at wileyonlinelibrary.com]

where $|\Omega_{i,j,k}|$ is the volume of cell $\Omega_{i,j,k}$. In a staggered grid some variables are not defined in the cell center, for example the velocities u, v and w, placed at the cell interfaces. Velocity should be interpreted as *average velocity* as

$$\begin{aligned} u_{i+\frac{1}{2},j,k} &= \frac{1}{\Delta x_{i+\frac{1}{2}}\Delta y_j \Delta z_k}\int_{x_i}^{x_{i+1}}\int_{y_{j-\frac{1}{2}}}^{y_{j+\frac{1}{2}}}\int_{z_{k-\frac{1}{2}}}^{z_{k+\frac{1}{2}}} u(x,y,z)\,dxdydz, && \text{with} && \Delta x_{i+\frac{1}{2}} = \frac{1}{2}\left(\Delta x_i + \Delta x_{i+1}\right),\\ v_{i,j+\frac{1}{2},k} &= \frac{1}{\Delta x_i \Delta y_{j+\frac{1}{2}}\Delta z_k}\int_{x_{i-\frac{1}{2}}}^{x_{i+\frac{1}{2}}}\int_{y_j}^{y_{j+1}}\int_{z_{k-\frac{1}{2}}}^{z_{k+\frac{1}{2}}} v(x,y,z)\,dxdydz, && \text{with} && \Delta y_{j+\frac{1}{2}} = \frac{1}{2}\left(\Delta y_j + \Delta y_{j+1}\right),\\ w_{i,j,k+\frac{1}{2}} &= \frac{1}{\Delta x_i \Delta y_j \Delta z_{k+\frac{1}{2}}}\int_{x_{i-\frac{1}{2}}}^{x_{i+\frac{1}{2}}}\int_{y_{j-\frac{1}{2}}}^{y_{j+\frac{1}{2}}}\int_{z_k}^{z_{k+1}} w(x,y,z)\,dxdydz, && \text{with} && \Delta z_{k+\frac{1}{2}} = \frac{1}{2}\left(\Delta z_k + \Delta z_{k+1}\right). \end{aligned}$$

2.2 | Subgrid

There is an important trade-off for numerical methods between accuracy and the time required for the computations. The introduction of a subgrid by Casulli in Reference 45 is an innovative method to improve computational performance substantially, while still maintaining very high accuracy. The main idea is to maintain the system size relatively small without compromising the accuracy of the computation of the water volume. To do so, two different grids are employed, one with coarse and one with finer resolution. The original mesh is where the free surface elevation $\eta = \eta(x,y,t)$ is defined; the latter (the subgrid) is used to hold the input data of the bottom elevation $b = b(x,y)$ and to compute the total water volume in each computational cell, as well as the face-averaged water depths $H = H(x,y,t)$. This separation allows for a faster algorithm because the operations on the subgrid require a lower computational effort and because the CFL condition acts on the coarser grid; meanwhile, volume accuracy is radically improved thanks to the subgrid, see Figure 2 for a sketch in 1D. In wet regions, the local water depth H, the bottom elevation b and the free surface elevation η are related via the linear relation $\eta = H + b$. In general, including dry areas but in the absence of floating objects, we have the nonlinear relation $H = \max(0, \eta - b) \geq 0$. For the sake of simplicity we present the concept in one space dimension only, and for the moment without the floating objects, which will be introduced later. We call the subgrid cells size $\Delta x_s = \Delta x / s$, where s is the number of subcells in each cell. Potentially, s could vary spatially, but it is assumed to be constant since there is no need to make distinctions at this point. The average water depth in a cell is computed as a sum of the water depth in each subcell:

$$H(\eta_i) = \frac{1}{\Delta x}\sum_s \max(0, \eta_i - b_{i,s}) \cdot \Delta x_s = \frac{1}{s}\sum_s \max(0, \eta_i - b_{i,s}), \tag{1}$$

since Δx_s is assumed to be constant. Since the grid is uniform, this depth function is closely related to the corresponding volume function through $V(\eta_i) = \Delta x \Delta y H(\eta_i)$. The free surface elevation is assumed to be piecewise constant per cell, so

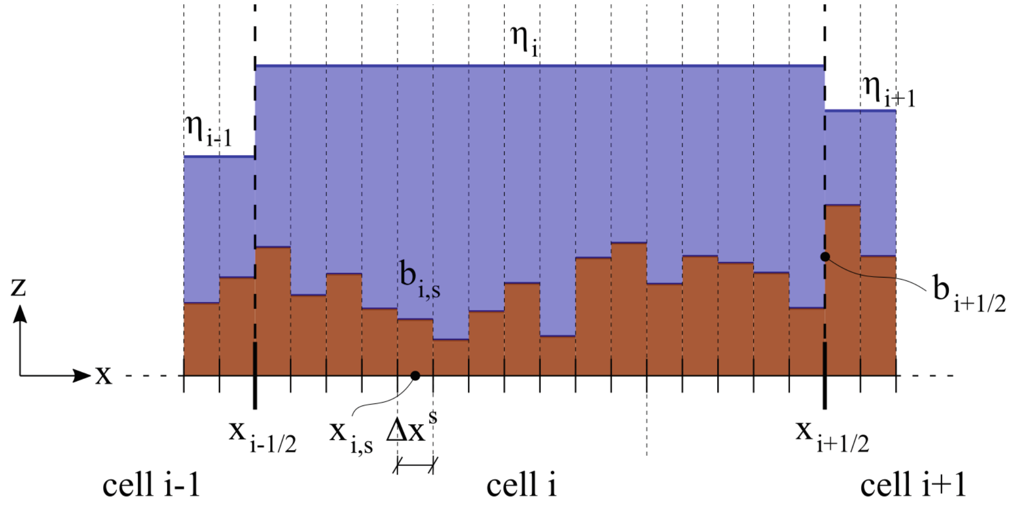

FIGURE 2 Cell divided in subcells [Colour figure can be viewed at wileyonlinelibrary.com]

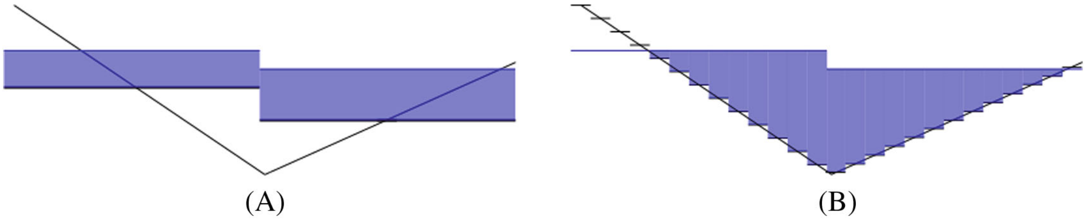

FIGURE 3 Volumes computed with the same number of cells with a simple grid (A) and with the addition of a subgrid (B). Oblique lines are the real bathymetry. The η is the same in both cases but the bathymetry can be more accurate with a subgrid. [Colour figure can be viewed at wileyonlinelibrary.com]

the subcell volumes in the summation differ only if the bottom elevation varies spatially at the subgrid level. The derivative of the average depth function is given by

$$H'(\eta_i) = \frac{1}{s}\sum_s H_s'(\eta_i, s), \qquad \text{with} \qquad H_s'(\eta_i, s) = \begin{cases} 1 & \text{if } \eta_i > b_{i,s} \\ 0 & \text{if } \eta_i \le b_{i,s} \end{cases}. \tag{2}$$

A visual representation of the improvements on volume computation is provided in Figure 3. In this example, a sloped bottom is discretized first on a 2 cells grid, and then on a 2 cells grid linked to a $s = 13$ subgrid. The free surface elevation is always the same. The subgrid substantially improves over the simple piecewise constant approximation of the bottom. Also, in the case without subgrid the cells are regarded either as dry or wet, while in the grid-subgrid case cells can be wet, dry or partially wet.

It is reasonable to spend some words on the similarities and differences between the use of a fine grid without subgrid and a coarse grid connected to an equally fine subgrid, see Figure 4 for a comparison. In the first case (fine grid without subgrid), each cell has an independently moving free surface, so accuracy is high; free surface waves profiles are more visible and wet/dry areas are more realistic. The price to pay for this is a very high amount of computations, which are time and memory consuming. This is due to the large number of unknowns (free surface elevations) and due to the small time step that is imposed by the CFL stability condition on a fine mesh. In the second case (coarse grid with subgrid) the flow in the domain is represented by a much smaller number of unknowns (free surface elevations), hence free surface wave profiles are less accurately resolved, but the decrease in accuracy is counterbalanced by a remarkable reduction of the unknowns and by a larger time step, since the CFL condition is only based on the mesh spacing of the grid and not on the spacing of the subgrid. At the aid of subgrid results are obtained much faster compared to a fine mesh simulation. A compromise has to be made to obtain a sufficiently accurate result in a reasonable time; to do so,

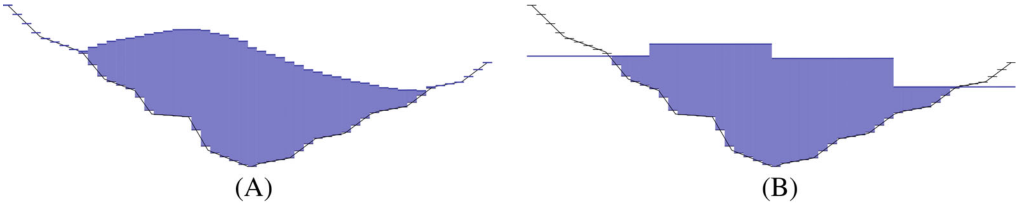

FIGURE 4 Differences between using only a fine grid (A) compared to a coarse grid with a subgrid (B). Δx on the left is equal to Δx_s on the right. [Colour figure can be viewed at wileyonlinelibrary.com]

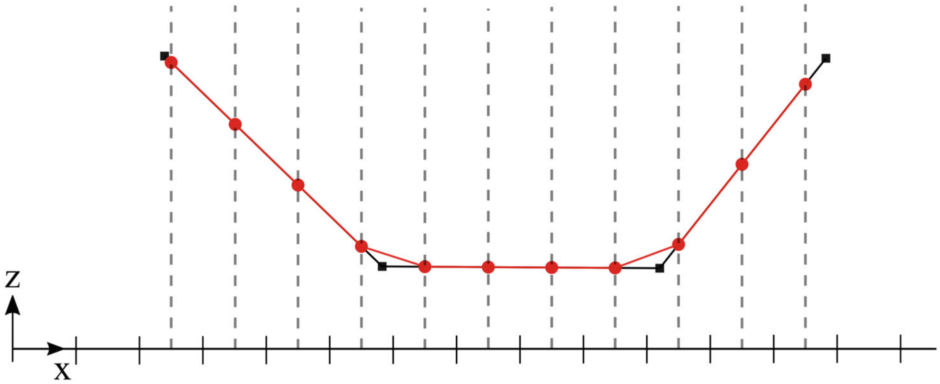

FIGURE 5 Illustration of the ship blueprint in 1D/2D$_{xz}$ and the interpolation on subgrid points [Colour figure can be viewed at wileyonlinelibrary.com]

the subgrid is an invaluable tool. Some small scale information may be lost, but if they are not required there is a lot to be gained in efficiency. The actual number of cells and subcells should take in consideration all these observations. A possible decisional process is the following:

1. Choose the subcells size based on the bottom variability (steep slopes and frequent ups and down require small Δx_s), so that volume is accurately computed. The total number of subcells in the domain is $N_{\text{subc}} = \dfrac{x_E - x_W}{\Delta x_s}$.
2. Choose $I_{\max}$ so that the free surface is accurate enough (depends on the purpose of the simulation); to help with the choice, one could simply start with a fairly small $I_{\max}$, run a few time steps of the simulation, observe the results and progressively increase it, if necessary.
3. Calculate $s = \dfrac{N_{\text{subc}}}{I_{\max}}$, rounded at the highest whole number. $I_{\max}$ and s are related: the smaller $I_{\max}$, the bigger s.

2.3 | Shape representation of floating objects on the subgrid and mass distribution

The representation of the ship is parametric: the $x-y-z$ coordinates of a finite set of points is expected as input, they are placed in the domain space (according to the center of mass position and orientations) and used as a blueprint to build the discretized ship, assuming they are connected by straight lines.

An algorithm has to be developed to find the intersections of the input hull with the vertical lines passing through every subcell center. Those intersection will approximate the hull with piecewise constant values. In 1D/2D$_{xz}$ simulations this reconstruction is exact, that is, it preserves the volume of ship, where the intersection is approximating only one segment. In the subcells with the input points, there are two segments with different orientations, and the intersection will be on only one segment, so the reconstruction is not exact there; provided a sufficiently fine subgrid, this effect is negligible. In Figure 5 is shown an example of interpolation in 1D/2D$_{xz}$; the input ship is defined by the black points, while the reconstructed ship is in red.

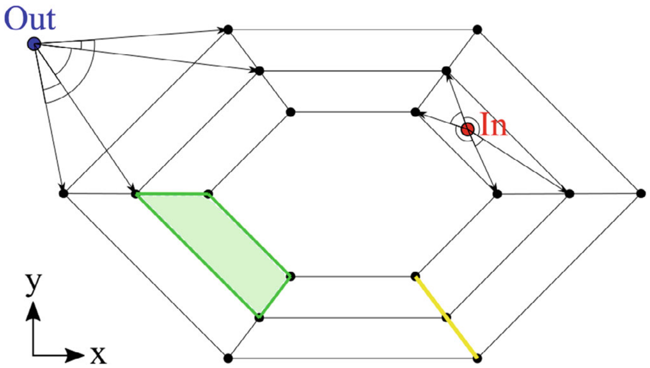

FIGURE 6 Illustration of the ship blueprint in 2D$_{xy}$/3D and the interpolation on subgrid points. The green lines highlight a quadrilateral, the yellow line is an edge. [Colour figure can be viewed at wileyonlinelibrary.com]

In 1D simulations with subgrid along y and in 2D$_{xy}$/3D simulations the idea of reconstruction is the same, but with the additional y dimension there are polygons instead of straight lines. Let us consider an example as shown in Figure 6 and follow the process steps. The input vessel is thought as composed of a series of horizontal layers, and the points are their intersections with the ship edges (an edge is highlighted in yellow); in the illustration there are 3 layers, each one with 6 points. Every close couple of points in a layer will form a quadrilateral (one is highlighted in green) with the corresponding couple on a next layer, except for the last one, which will be a generic polygon. At every time step, we are interested in finding the z elevation of the hull in the $(x, y)_{\text{sub}}$ subcells centers; Since the coordinates of the ship points $(x, y)_{\text{ship}}$ almost never coincide with the subcells centers, an interpolation from the blueprint is necessary. A 2D$_{xy}$/3D algorithm carries out the following operations:

1. The portion of the subgrid surrounding the ship footprint (the projection of the ship points in the $x - y$ plane) is cropped out to avoid unnecessary computations where they are surely not needed
2. Each subgrid point p_{sub} (in Figure 6, the blue and red points are two examples) is tested to determine if it is inside or outside the footprint. To do so, one can start, for all the vessel polygons, by drawing the vectors connecting their vertices with the point p_{sub} and storing them. Then, the scalar product of all the possible ordered couples of vectors is done to compute the angles between them. If the sum of these angles is $< 2\pi$ the point is out, if it is $= 2\pi$ it is in the polygon. Practically, it is necessary to ease a bit these rules because the angles are computed with a finite precision so there are some errors: p_{sub} is considered inside if the sum of the angles is $\geq 2\pi - \xi$, with ξ a small number (like $2\pi/1000$, it may be adjusted based on the subgrid size)
3. Once the polygon surrounding p_{sub} is determined, it is possible to compute the vector $n = (n_x, n_y, n_z)$ orthogonal to the plane described by two polygon edges. The vertex between the two edges has coordinates $v = (x_v, y_v, z_v)$. The elevation of the hull in that subcell $l_{p_{\text{sub}}}$ is then:

$$l_{p_{\text{sub}}} = z_v - \frac{1}{n_z} \left[n_x (x_{p_{\text{sub}}} - x_v) + n_y (y_{p_{\text{sub}}} - y_v) \right] \tag{3}$$

With these operations, the input ship is reconstructed where it is needed, in the subcells centers. Interestingly, even when the water flow is 1D it is possible to use the subgrid to have a 3D representation of the ship and improve volume computations.

The mass distribution on the ship determines where the center of mass is located and so, together with the pressure on the hull, it has a major role in the stability of the vessel. As a general rule, an unstable configuration is one with G high along the vertical and skewed on the port or starboard; once it starts rolling, the torque amplifies the rotational velocity and the ship capsizes. The mass distribution of the floating object is given at the start of the simulation and then kept constant. Thus, in a body-fixed frame of reference also the inertia I is constant. For convenience, in the test cases of Section 3 we used simplifying assumptions on where the mass is located. For applications with real ships, it would be better to remove those assumptions and use the available data on the structure and on the heavy equipment onboard. The following procedure describes how to generate an object with heterogeneous mass distribution:

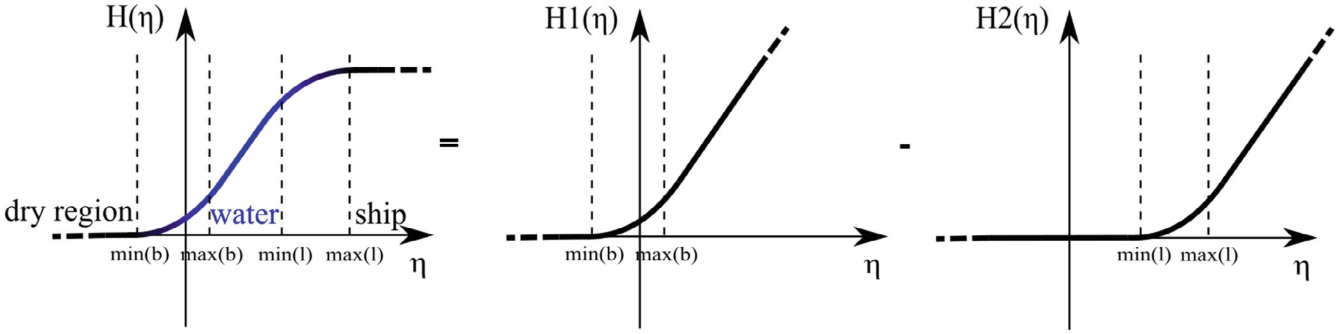

FIGURE 7 Schematic representation of the average depth functions H, H_1 and H_2. Smoothness is a consequence of the subgrid, as each cell can also be partially wet. [Colour figure can be viewed at wileyonlinelibrary.com]

1. Take the input ship rotated in upright position.
2. Apply the discretization of the hull at subgrid level (as seen in Section 2.3). Now it is possible to imagine the vessel as formed by a sequence of vertical stripes which are bounded below by the hull and above by the deck. Here we define the deck based on the highest elevation reached by the hull.
3. Assign at every stripe a share of the total mass m_s; this controls the horizontal position of the global center of mass G. If the distribution is known it is possible to define the mass of each stripe manually; if unknown, a simple assumption is to set the masses proportional to the vertical lengths of the stripes.
4. Assign at every stripe the vertical position of its center of mass; this controls the z position of the global center of mass. If it is not known, one could place it always at the same adimensional height: for example if the mass is homogeneously distributed the center will be at 1/2 of the stripe vertical length.
5. Compute the global center of mass G and place there the origin of the body-fixed frame of reference $x'z'$.
6. Compute the moment of inertia of the ship I_s using

$$I = \sum_{s} m_{s,s} \left(x'^2_s + z'^2_s\right). \tag{4}$$

The above procedure allows to have an heterogeneous mass distribution at the finest level of accuracy allowed by the subgrid resolution. It is also extendable to 3D simulations with the due changes (the stripes are now prisms and inertia is a 3x3 tensor).

The fluid-structure interaction problem imposes one more limitation to the volume in each cell, which should be bounded from above at the current elevation of the hull $\boldsymbol{l}$. The depth function is therefore also dependent on the position and orientation of the ship, which moves at each time step:

$$H(\eta_i, x_G, z_G, \varphi) = \frac{1}{s} \sum_{s} \max\left(0, \min(\eta_i - b_{i,s}, l_{i,s} - b_{i,s})\right) = H_1 - H_2. \tag{5}$$

where the Jordan decomposition of H is needed for the nested Newton algorithm of Casulli and Zanolli[43,44] that will be used later in this article. An illustration of the relationship between H, H_1, and H_2 is provided in Figure 7.

Figure 8 illustrates how the average water depths are computed on the subgrid in the presence of a floating rigid body. The considerations concerning the use of the subgrid for the vessel reconstruction are analogous to those made before for the bottom resolution on the subgrid for the hydrodynamics. Of course now the total number of subcells has also to be adjusted to discretize with enough accuracy the geometry of the ship, not only the bottom topography. A major difference between the vessel and the bottom is that the former is moving at each time step; the elevation of the hull $\boldsymbol{l}$ is sampled at the intersection of said hull with the vertical passing through the center of the subcells, so in general the hull is not discretized in the same points. This reconstruction maximizes the accuracy of the water volume computation and allows to have the piecewise constant hull $\boldsymbol{l}$ always aligned with the piecewise constant bathymetry $\boldsymbol{b}$. The ship is discretized by a finite number of subcells, which is proportional to the area of the projection of the vessel in the horizontal plane. This may cause some problems when the floating body has almost vertical sides (usually at the external part) because there may not be an adequate number of subcells for them, or none at all (depending on the orientation of the ship and the

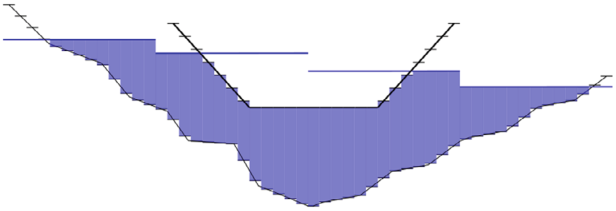

FIGURE 8 Volume computation around a floating ship. In this example the domain is divided in four cells (thus there are four η) and each cell has 13 subcells. [Colour figure can be viewed at wileyonlinelibrary.com]

subcells size); the volume computation would not be significantly affected, but the horizontal forces would be. For this case a different approach to forces computation could be explored, sampling them in a constant number of points spread evenly on the hull, regardless of the orientation or the subgrid.

With the present definition of the algorithm, it is not possible to simulate a completely immersed body since the free surface is defined by a single-valued function, so it is not possible to have water above the object.

2.4 | 1D model

We first introduce the new method for the simple one-dimensional case, in order to ease notation and to simplify the overall presentation, allowing to focus on the new main ingredients of the approach. Subsequently, we will then show the new method for the general three-dimensional case.

2.4.1 | Shallow water equations

The shallow water equations are the starting point for our numerical model. They can be derived from depth-averaging of the incompressible Navier-Stokes equations, which describe the flow of an incompressible fluid with constant density, while conserving mass and linear momentum. Assuming that the flow is *hydrostatic* the equations simplify and become computationally much easier to solve; this assumption is valid when the vertical accelerations and the vertical viscosity are significantly smaller than the gravity acceleration and pressure gradient, which is usually true for geophysical flows. The one-dimensional shallow water equations with bottom friction read

$$\frac{\partial H(\eta)}{\partial t} + \frac{\partial q}{\partial x} = 0, \tag{6a}$$

$$\frac{\partial q}{\partial t} + \frac{\partial uq}{\partial x} + gH\frac{\partial \eta}{\partial x} = -\gamma q, \tag{6b}$$

where $g = 9.81$ m/s^2 is the gravity constant, $u = u(x,t)$ is the average velocity, $H = H(x,t)$ is the water depth, $b = b(x)$ the bottom topography and $q = H \cdot u$ is the discharge. $\eta(x,t) = b(x) + H(x,t) + P_s(x,t)$ is the free surface elevation plus an additional height accounting for the pressure acting on the floating body, which is $P_s(x,t) = 0$ outside the body region. A typical dimensionless number appearing in shallow water flows is the Froude number $\mathrm{Fr} = |u|/\sqrt{(gH)}$, which allows to distinguish subcritial flows from supercritical ones. In the system above, $\gamma = \gamma(H,u)$ is a nonnegative bottom friction coefficient that can be defined for example, using the Strickler parameter k_s and the hydraulic radius R_h. In the engineering practice, for wide channels where one can assume $R_h \approx H$ one obtains

$$\gamma = \frac{g \cdot |q|}{k_s^2 \cdot R_h^{\frac{1}{3}} \cdot H^2} \approx \frac{g \cdot |q|}{k_s^2 \cdot H^{\frac{7}{3}}}. \tag{7}$$

If the roughness is known from a Manning coefficient n or a Chézy coefficient χ, the formula (7) is still valid, since the following relations hold:

$$k_s = \frac{1}{n} = \chi R_h^{-\frac{1}{6}}. \tag{8}$$

Typical values for n in an open channel can be found for example in Chow.[49]

2.4.2 | Dynamics of floating rigid bodies

Before coupling the floating rigid bodies (ships) with the flow dynamics, it is useful to specify how their kinematics and dynamics is handled, as well as their shape and mass distribution. A ship is treated as a rigid body with total mass m_s. It is convenient to define a body-fixed frame of reference $x'z'$, with the origin in its center of mass $G = (x_G, z_G)$, as shown in Figure 9; x' lies on the longitudinal axis of the vessel and is responsible for surge motion, while z' ($\perp x'$) points up toward the sky and is responsible for heave motion. Only one point is needed to track the ship position, all the others can be derived starting from the known one; this special point is set to be the center of mass. In 1D and 2D$_{xz}$ simulations the vessel has three degrees of freedom, two for translation along the horizontal and vertical axes x and z, one for the rotation around the y axis. The orientation of the object in the space is represented by the angle φ, defined as the angle between axes z and z'. The equations that govern the movement are derived from the conservation of linear and angular momentum:

$$m_s \frac{du_G}{dt} = \sum F_{x,s}, \tag{9a}$$

$$m_s \frac{dw_G}{dt} = -m_s g + \sum F_{z,s}, \tag{9b}$$

$$\frac{d}{dt} I_s \dot{\varphi} = \tau, \tag{9c}$$

and from the definitions of the linear and angular velocities

$$\frac{dx_G}{dt} = u_G, \tag{10a}$$

$$\frac{dz_G}{dt} = w_G, \tag{10b}$$

$$\frac{d\varphi}{dt} = \dot{\varphi}. \tag{10c}$$

In the equations of motion m_s is the ship mass and I_s is the ship's moment of inertia relative to G, constant in the body-fixed reference frame and given by (4). The forces acting on the vessel are those generated by gravity F_g (always vertical) and the hydrostatic pressure orthogonal to the hull, which creates a horizontal and a vertical component of the force F_x and F_z. The ship will then be able to float and passively being carried by an imbalance in the free surface; also, these forces will create a torque that will make the ship oscillate. At this stage of development of the model, the propulsion force and the steering moment are not considered, but we only consider the following forces:

$$F_{x,s} = \rho g \, \max(0, \eta_s - l_s) \, \Delta x_s \, \tan(\alpha_s), \quad F_{z,s} = \rho g \, \max(0, \eta_s - l_s) \, \Delta x_s, \quad \tau = \sum_s \left[F_{x,s}(l_s - z_G) + F_{z,s}(x_G - x_s) \right], \tag{11}$$

where ρ is the water density, l_s is the hull elevation at the subcell s center, α_s is the smallest angle between the horizontal and a vector orthogonal to the hull in that subcell, x_s is the x coordinate of the subcell s center.

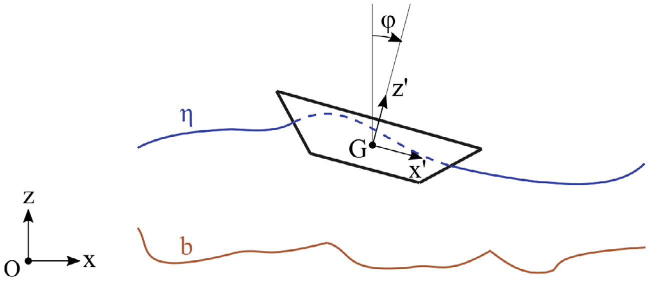

FIGURE 9 General 1D/2D$_{xz}$ scheme of the ship motion problem [Colour figure can be viewed at wileyonlinelibrary.com]

2.4.3 | Semi-implicit discretization

The equations of motion of the rigid body (9)–(10) provide the accelerations that are necessary to compute changes in the ship position, orientation and velocities. At the beginning of each time step, they are updated using an explicit second order accurate Taylor method:

$$x_G^{n+1} = x_G^n + u_G^n \cdot \Delta t + \frac{1}{2}\frac{\sum_s F_{x,s}^n}{m_s} \cdot \Delta t^2, \tag{12a}$$

$$z_G^{n+1} = z_G^n + w_G^n \cdot \Delta t + \frac{1}{2}\frac{\sum_s F_{z,s}^n - F_g}{m_s} \cdot \Delta t^2, \tag{12b}$$

$$\varphi^{n+1} = \varphi^n + \dot{\varphi}^n \Delta t + \frac{1}{2}\frac{\tau^n}{I}\Delta t^2, \tag{12c}$$

$$u_G^{n+1} = u_G^n + \frac{\sum_s F_{x,s}^n}{m_s} \cdot \Delta t, \tag{12d}$$

$$w_G^{n+1} = w_G^n + \frac{\sum_s F_{z,s}^n - F_g}{m_s} \cdot \Delta t, \tag{12e}$$

$$\dot{\varphi}^{n+1} = \dot{\varphi}^n + \frac{\tau^n}{I}\Delta t. \tag{12f}$$

With the notation $f = q \cdot u = H \cdot u^2$, a semi-implicit discretization of the 1D shallow water system (6) can be written as:

$$H_i\left(\eta_i^{n+1}, x_G^{n+1}, z_G^{n+1}, \varphi^{n+1}\right) = H(\eta_i^n, x_G^n, z_G^n, \varphi^n) - \frac{\Delta t}{\Delta x}\left(q_{i+\frac{1}{2}}^{n+1} - q_{i-\frac{1}{2}}^{n+1}\right), \tag{13a}$$

$$q_{i+\frac{1}{2}}^{n+1} = q_{i+\frac{1}{2}}^{*} - \frac{\Delta t}{\Delta x} g H_{i+\frac{1}{2}}^n \left(\eta_{i+1}^{n+1} - \eta_i^{n+1}\right) - \Delta\gamma_{i+\frac{1}{2}}^n q_{i+\frac{1}{2}}^{n+1}. \tag{13b}$$

The fluxes in the mass conservation equation, the pressure gradient in the momentum equation and the bottom friction term are discretized implicitly, while the nonlinear convective terms are discretized in an explicit manner. In order to avoid nonlinearities in the implicit part, the water depth at the cell interface $H_{i+\frac{1}{2}}^n$ is taken explicitly, as well as the bottom friction coefficient $\gamma_{i+\frac{1}{2}}^n$. For subcritical flows (Fr ≤ 1) it $H_{i+\frac{1}{2}}^n$ is taken equal to the average of the water depths H_i^n and H_{i+1}^n, while for supercritical flows (Fr > 1) we use the upwind water depth, hence

$$H_{i+\frac{1}{2}}^n = \begin{cases} \dfrac{H_i^n + H_{i+1}^n}{2} & \text{if Fr} \leq 1, \\ H_i^n & \text{if Fr} > 1 \text{ and } q_{i+\frac{1}{2}} > 0, \\ H_{i+1}^n & \text{if Fr} > 1 \text{ and } q_{i+\frac{1}{2}} < 0. \end{cases} \tag{14}$$

The term $q_{i+\frac{1}{2}}^{*}$ contains the explicit discretization of the nonlinear convective terms:

$$q_{i+\frac{1}{2}}^{*} = q_{i+\frac{1}{2}}^{n} - \frac{\Delta t}{\Delta x}\left(f_{i+1} - f_i\right). \tag{15}$$

The fluxes in Equation (15) are approximated by a simple arithmetic mean of the momentum-conservative Stelling&Duinmeijer flux[50] and the shock-capturing Rusanov flux:[51]

$$f_i = \frac{f_i^{SD} + f_i^{R}}{2}, \tag{16}$$

where

$$f_i^{SD} = \frac{q_{i+\frac{1}{2}}^n + q_{i-\frac{1}{2}}^n}{2} u_{i+1}^{\text{upwind}}, \quad \text{with} \quad u_i^{\text{upwind}} = \begin{cases} u_{i-\frac{1}{2}}^n & \text{if } \frac{q_{i+\frac{1}{2}}^n + q_{i-\frac{1}{2}}^n}{2} > 0 \\ u_{i+\frac{1}{2}}^n & \text{if } \frac{q_{i+\frac{1}{2}}^n + q_{i-\frac{1}{2}}^n}{2} \leq 0 \end{cases} \tag{17}$$

and

$$f_i^R = \frac{1}{2}\left(f^n_{i+\frac{1}{2}} + f^n_{i-\frac{1}{2}}\right) - \frac{1}{2}s_i^{\max}\left(q^n_{i+\frac{1}{2}} - q^n_{i-\frac{1}{2}}\right), \tag{18}$$

with the wave speed estimate

$$s_i^{\max} = 2 \cdot \max\left(\left|u^n_{i+\frac{1}{2}}\right|, \left|u^n_{i-\frac{1}{2}}\right|\right) + c. \tag{19}$$

The product $2u$ in Equation (19) is the system eigenvalue emerging from a characteristic analysis; see Reference 39. The term c is a small constant, for example, 0.1, whose purpose is to always force the wave speed to be nonzero even for $u = 0$, so the unstable central flux is avoided. The time step size Δt is adjusted at every time iteration and it is based on the Courant–Friedrichs–Lewy (CFL) condition to assure stability:[52]

$$\Delta t = \min\left(\Delta t_{\max}, \frac{\text{CFL} \cdot \Delta x}{2|u|_{\max} + c}\right) \qquad \text{with} \qquad \text{CFL} = 0.9. \tag{20}$$

A small constant has been introduced in the denominator to avoid division by 0 in the case of still water. A maximum for the time step size can also be set if accuracy requires it. The discretized system (13) can be reduced by eliminating the unknown variables q in the mass equation through substitution from the momentum equation:

$$\begin{aligned} &H_i\left(\eta_i^{n+1}, x_G^{n+1}, z_G^{n+1}, \varphi^{n+1}\right) - \frac{\Delta t^2}{\Delta x^2}\left(\frac{gH^n_{i+\frac{1}{2}}}{1+\Delta t\,\gamma^n_{i+\frac{1}{2}}}\left(\eta^{n+1}_{i+1} - \eta^{n+1}_i\right) - \frac{gH^n_{i-\frac{1}{2}}}{1+\Delta t\,\gamma^n_{i-\frac{1}{2}}}\left(\eta^{n+1}_i - \eta^{n+1}_{i-1}\right)\right) \\ &= H_i\left(\eta_i^n, x_G^n, z_G^n, \varphi^n\right) - \frac{\Delta t}{\Delta x}\left(\frac{q^*_{i+\frac{1}{2}}}{1+\Delta t\,\gamma^n_{i+\frac{1}{2}}} - \frac{q^*_{i-\frac{1}{2}}}{1+\Delta t\,\gamma^n_{i-\frac{1}{2}}}\right). \end{aligned} \tag{21}$$

The resulting mildly nonlinear system, which now contains the free surface at the new time as the only unknown can be easily solved at the aid of a (nested) Newton method, see References 41-44.

In the final mildly nonlinear pressure system (21) the location of the ship at the old and new time levels affects the calculation of the water volume in each cell, and the water exerts pressure forces on the hull which are taken into account in the discretized ODE system of the rigid body dynamics (12), so the fluid and the structure are coupled.

2.5 | 2Dxz model

The model described in Section 2.4 is applicable in 1D, and for some simplified cases a 1D approach may be sufficient. However, many real applications require the extension to higher dimensions and more details about the velocities. In this section and in the subsequent Section 2.7, the 2D_{xz} and 3D models are presented, together with the description of their most relevant characteristics. Attention will be directed to what is new compared to the 1D case.

The 2D_{xz} model has one horizontal and one vertical dimension, so the domain is a vertical section discretized on a grid of $I_{\max} \cdot K_{\max}$ cells, whose size is $\Delta x \cdot \Delta z_k$ each. The grid is staggered, so the vertical velocity w is defined at the interface with the cell above or below (see Figure 10). The free surface elevation $\eta(t, x)$ and the bathymetry $b(x)$ can vary spatially only moving in the horizontal direction, so they are the same along a vertical column of the grid. All the variables represent lateral averages. In the mass conservation equation the difference of fluxes has to take into account all the different horizontal velocities along the vertical, so on each interface the flux is computed with an integral. The momentum equation has a new advective term and the viscosity along the vertical is added; the horizontal viscosity is neglected because, with the assumption of shallow water, it is usually fair to say that $(\nu u_z)_z \gg (\nu u_x)_x$. The γ factor is still

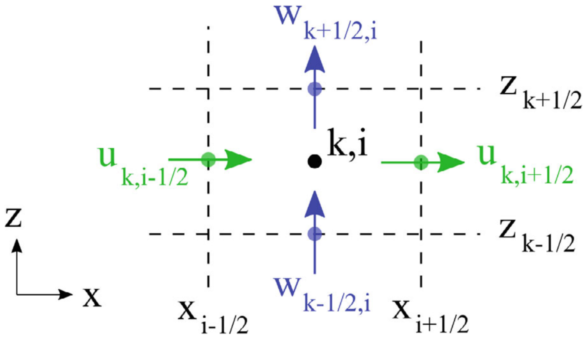

FIGURE 10 Grid in the $2D_{xz}$ model [Colour figure can be viewed at wileyonlinelibrary.com]

present for the lateral friction. With the vertical velocity as new unknown, the system needs one more equation, stating that the divergence of the flow velocity is zero.

$$\frac{\partial}{\partial t}[H(\eta)] + \frac{\partial}{\partial x}\left[\int_b^\eta u(x,z,t)dz\right] = 0, \tag{22a}$$

$$\frac{\partial u}{\partial t} + \frac{\partial(uu)}{\partial x} + \frac{\partial(uw)}{\partial z} + g\frac{\partial \eta}{\partial x} = \frac{\partial}{\partial z}\left(\nu\frac{\partial u}{\partial z}\right) - \gamma u, \tag{22b}$$

$$\frac{\partial u}{\partial x} + \frac{\partial w}{\partial z} = 0. \tag{22c}$$

The momentum equation in system (22) is written before integration along the vertical, therefore the unknown is the primitive variable u. Only after the integration $\int u(x,z)dz = q$ the conserved variable appears, see also References 53. In this article, we make use of z-layers, hence the integral in the first equation of (22) is discretized as follows:

$$\int_b^\eta u(x,z)dz \approx \sum_k q_{i+\frac{1}{2},k} = \sum_k \Delta z_{i+\frac{1}{2},k} u_{i+\frac{1}{2},k}, \qquad k = 1, 2, \ldots, K_{\max}. \tag{23}$$

The vertical mesh spacing depends on the local bottom and on the free surface elevation. More specifically we choose $\Delta z_k = \Delta z$ for all cells that are completely included between b and η, while the length of cells adjacent to the bottom and the free surface are adjusted (as presented in Figure 11), so that

$$\sum_k \Delta z_{i+\frac{1}{2},k} = H_{i+\frac{1}{2}} = \max\left(0, \min\left(\eta_{i+\frac{1}{2}} - b_{i+\frac{1}{2}}, l_{i+\frac{1}{2}} - b_{i+\frac{1}{2}}\right)\right). \tag{24}$$

The advective term $\partial(qu)/\partial x$ is discretized in the same fashion as described in Section 2.4.3. Instead, for the advective term with mixed velocities we apply a central scheme. Particular care is needed because the product is defined at the corners of the cell, but on the staggered grid none of the factors are there; some sort of average is needed. The discretization is done using the arithmetic mean of the velocity and linear momentum at time n, as written in Equation (25) and illustrated in Figure 12:

$$\frac{\partial(qw)}{\partial z} \approx \frac{1}{\Delta z}\left(\frac{q^n_{i+\frac{1}{2},k+1} + q^n_{i+\frac{1}{2},k}}{2}\right)\left(\frac{w^n_{i+1,k+\frac{1}{2}} + w^n_{i,k+\frac{1}{2}}}{2}\right) - \frac{1}{\Delta z}\left(\frac{q^n_{i+\frac{1}{2},k} + q^n_{i+\frac{1}{2},k-1}}{2}\right)\left(\frac{w^n_{i+1,k-\frac{1}{2}} + w^n_{i,k-\frac{1}{2}}}{2}\right) \tag{25}$$

Because the advective term (25) is explicit, it is added to the definition of q^*.

The introduction of the vertical viscosity requires boundary conditions due to stresses applied on the boundaries, for example, roughness or wind stress. Indeed, at the vertical water boundaries the product $\nu\partial u/\partial z$ is substituted by the boundary conditions:

$$\begin{cases} \nu\frac{\partial u}{\partial z} = \gamma_T(u^a - u^s) & \text{at the free surface} \\ \nu\frac{\partial u}{\partial z} = \gamma_B u^b & \text{at the bottom} \end{cases}, \quad \text{with} \quad \gamma_T = C_d\frac{\rho_a}{\rho}|u^a|, \quad \gamma_B = \frac{g|u^b|}{k_s^2 R_h^{1/3}}, \tag{26}$$

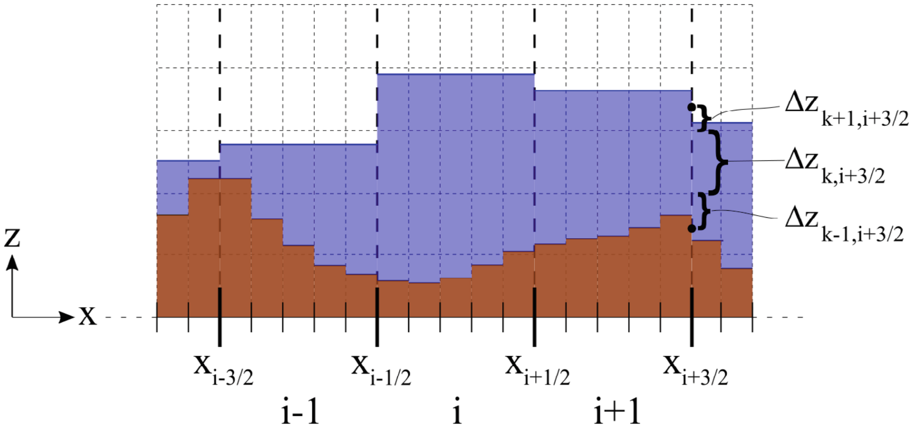

FIGURE 11 General 2D$_{xz}$ scheme, showing the Δz_k at the interface $i+\frac{3}{2}$ [Colour figure can be viewed at wileyonlinelibrary.com]

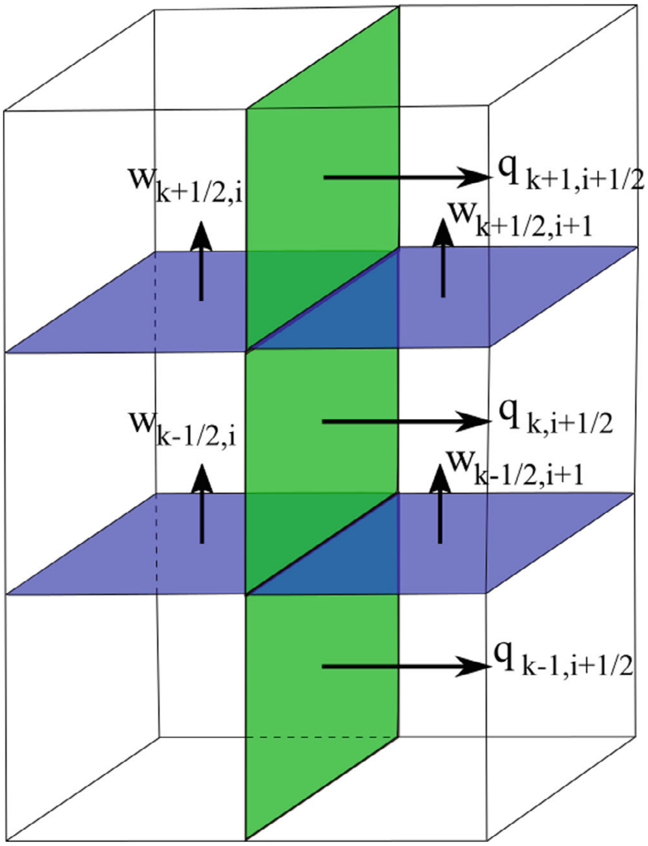

FIGURE 12 Illustration of terms in the mixed velocities product on a staggered grid [Colour figure can be viewed at wileyonlinelibrary.com]

where ν is the kinematic viscosity coefficient, C_d is a drag coefficient, $\rho_a = 1.25\,\mathrm{kg/m^3}$ is the air density, u^a is the horizontal component of the wind speed, u^s and u^b are the horizontal component of the water velocity at the surface and at the bottom, respectively. Viscosity is treated as an implicit term:

$$\frac{\partial}{\partial z}\left(\Delta z \nu \frac{\partial u}{\partial z}\right) \approx \frac{1}{\Delta z^n_{i+\frac{1}{2},k}}\left[\nu^{n+1}_{i+\frac{1}{2},k+\frac{1}{2}}\left(u^{n+1}_{i+\frac{1}{2},k+1} - u^{n+1}_{i+\frac{1}{2},k}\right) - \nu^{n+1}_{i+\frac{1}{2},k-\frac{1}{2}}\left(u^{n+1}_{i+\frac{1}{2},k} - u^{n+1}_{i+\frac{1}{2},k-1}\right)\right]. \tag{27}$$

Due to the viscosity, each momentum equation requires the neighbor velocities, so it not possible to simply do a substitution in the mass equation as was done in the 1D model. The matrix form of system (22) (the incompressibility equation is not needed at the moment) is:

$$H\left(\eta_i^{n+1}, x_G^{n+1}, z_G^{n+1}, \varphi^{n+1}\right) = H\left(\eta_i^{n}, x_G^{n}, z_G^{n}, \varphi^{n}\right) - \frac{\Delta t}{\Delta x}\left[\left(\boldsymbol{\Delta Z}_{i+\frac{1}{2}}\right)^T \boldsymbol{U}_{i+\frac{1}{2}}^{n+\theta} - \left(\boldsymbol{\Delta Z}_{i+\frac{1}{2}}\right)^T \boldsymbol{U}_{i-\frac{1}{2}}^{n+\theta}\right], \tag{28a}$$

$$\boldsymbol{A}_{i+\frac{1}{2}}^{n} \boldsymbol{U}_{i+\frac{1}{2}}^{n+1} = \boldsymbol{G}_{i+\frac{1}{2}}^{n} - g\frac{\Delta t}{\Delta x}\left(\eta_{i+1}^{n+\theta} - \eta_i^{n+\theta}\right) \boldsymbol{\Delta Z}_{i+\frac{1}{2}}^{2}, \tag{28b}$$

where $\theta \geq \frac{1}{2}$ is an implicitness factor (theta method), $\boldsymbol{\Delta Z}^2_{i+\frac{1}{2}}$ is the vector with the squared wetted distances along the vertical at time n, $\boldsymbol{U}^{n+1}_{i+\frac{1}{2}}$ is for the unknown horizontal velocities, $\boldsymbol{A}^n_{i+\frac{1}{2}}$ is a square symmetric tridiagonal matrix, $\boldsymbol{G}^n_{i+\frac{1}{2}}$ is the vector with all the explicit terms. The equations are computed only in the nondry cells of the domain column (to avoid unnecessary calculations), so on the vertical cells $k = m_{i+\frac{1}{2}}, m_{i+\frac{1}{2}}+1, \ldots, M^n_{i+\frac{1}{2}}$. Start index $m_{i+\frac{1}{2}}$ is only spatially variable according to the bottom elevation, while end index $M^n_{i+\frac{1}{2}}$ is spatially variable and time dependent according to the free surface current position and the bathymetry.

$$\boldsymbol{\Delta Z}^2 = \begin{pmatrix} \Delta z_M^2 \\ \Delta z_{M-1}^2 \\ \vdots \\ \Delta z_m^2 \end{pmatrix}, \qquad \boldsymbol{U} = \begin{pmatrix} u_M \\ u_{M-1} \\ \vdots \\ u_m \end{pmatrix}, \qquad \boldsymbol{G}^n = \begin{pmatrix} \Delta z_M q_M^* + \Delta t \gamma_T \Delta z_M u_a \\ \Delta z_{M-1} q_{M-1}^* \\ \vdots \\ \Delta z_m q_m^* \end{pmatrix} \tag{29}$$

$$\boldsymbol{A} = \begin{pmatrix} d_M + a_{M-\frac{1}{2}} + \gamma_T \Delta t \Delta z_M & -a_{M-\frac{1}{2}} & 0 & \ldots & 0 \\ -a_{M-\frac{1}{2}} & d_{M-1} + a_{M-\frac{1}{2}} + a_{M-\frac{3}{2}} & -a_{M-\frac{3}{2}} & & \\ \vdots & \vdots & \vdots & & \\ 0 & 0 & & -a_{m+\frac{1}{2}} & d_m + a_{m+\frac{1}{2}} + \gamma_B \Delta t \Delta z_m \end{pmatrix} \tag{30}$$

with $d_k = \Delta z_k^2 + \gamma_k \Delta t \Delta z_k$ and $a_{k\pm\frac{1}{2}} = \Delta t \nu_{k\pm\frac{1}{2}}$, $k = m, m+1, \ldots, M$. The substitution of the momentum equation in the mass equation and use of the abbreviation $H_i^n = H(\eta_i^n, x_G^n, z_G^n, \varphi^n)$ lead to:

$$H_i^{n+1} - g\frac{\Delta t^2}{\Delta x^2}\left\{\left(\theta \boldsymbol{\Delta} Z^T \boldsymbol{A}^{-1} \boldsymbol{\Delta Z^2}\right)^n_{i+\frac{1}{2}} \left[(\theta\eta)^{n+1}_{i+1} - (\theta\eta)^{n+1}_{i}\right] - \left(\theta \boldsymbol{\Delta} Z^T \boldsymbol{A}^{-1} \boldsymbol{\Delta Z^2}\right)^n_{i-\frac{1}{2}} \left[(\theta\eta)^{n+1}_{i} - (\theta\eta)^{n+1}_{i-1}\right]\right\} = r_i^n \tag{31}$$

with

$$\begin{aligned} r_i^n = H_i^n &- \frac{\Delta t}{\Delta x}\left[\left(\theta \boldsymbol{\Delta} Z^T \boldsymbol{A}^{-1} \boldsymbol{G}\right)^n_{i+\frac{1}{2}} - \left(\theta \boldsymbol{\Delta} Z^T \boldsymbol{A}^{-1} \boldsymbol{G}\right)^n_{i-\frac{1}{2}}\right] - \frac{\Delta t}{\Delta x}\left\{\left[(1-\theta)\,\boldsymbol{\Delta} Z^T \boldsymbol{U}\right]^n_{i+\frac{1}{2}} - \left[(1-\theta)\,\boldsymbol{\Delta} Z^T \boldsymbol{U}\right]^n_{i-\frac{1}{2}}\right\} \\ &+ g\frac{\Delta t^2}{\Delta x^2}\left\{\left(\theta \boldsymbol{\Delta} Z^T \boldsymbol{A}^{-1} \boldsymbol{\Delta Z^2}\right)^n_{i+\frac{1}{2}}\left[((1-\theta)\,\eta)^n_{i+1} - ((1-\theta)\,\eta)^n_{i}\right] - \left(\theta \boldsymbol{\Delta} Z^T \boldsymbol{A}^{-1} \boldsymbol{\Delta Z^2}\right)^n_{i-\frac{1}{2}}\left[((1-\theta)\,\eta)^n_{i} - ((1-\theta)\,\eta)^n_{i-1}\right]\right\}. \end{aligned} \tag{32}$$

It is important to notice that it is never necessary to compute the inverse $\boldsymbol{A}^{-1}$, because the products $\boldsymbol{A}^{-1}\boldsymbol{\Delta Z}^2$ and $\boldsymbol{A}^{-1}\boldsymbol{G}$ can be obtained solving the systems $\boldsymbol{AB} = \boldsymbol{\Delta Z}^2$ and $\boldsymbol{AC} = \boldsymbol{G}$, using the Thomas algorithm for tridiagonal systems.

Starting from Equation (31) it is possible to solve the system for $\boldsymbol{\eta}^{n+1}$ with the nested Newton method of Casulli and Zanolli. The size of this system is determined by the horizontal resolution, because the vertical one intervenes only during the assembly of its coefficients; this feature is very advantageous for numerical efficiency, also in the fully 3D case for predominantly horizontal flows, so it is possible to easily increase the vertical resolution at reasonable computational costs. With the solution $\boldsymbol{\eta}^{n+1}$, the velocities are computed from the solution of the $I_{\max}$ linear systems formed by the momentum equations written in matrix form, making use of the already known products $\boldsymbol{A}^{-1}\boldsymbol{\Delta Z}^2$ and $\boldsymbol{A}^{-1}\boldsymbol{G}$. The vertical velocities are obtained *a posteriori* from the incompressibility equation. Starting from the bottom with $w^{n+1}_{m-\frac{1}{2},i} = 0$, the others are found one after the other:

$$w^{n+1}_{i,k+\frac{1}{2}} = w^{n+1}_{i,k-\frac{1}{2}} - \frac{\Delta z^n_{i+\frac{1}{2},k} u^{n+1}_{i+\frac{1}{2},k} - \Delta z^n_{i-\frac{1}{2},k} u^{n+1}_{i-\frac{1}{2},k}}{\Delta x} \quad k = m_i, m_i+1, \ldots, M_i^n - 1. \tag{33}$$

An interesting aspect of this formulation of the algorithm is that for $K_{\max} = 1$ it automatically reduces to the $1D$ model previously described.

2.6 | Ship dynamics in three space dimensions

When the grid or the subgrid expands in both the x and y directions, it is possible to place in the domain a three-dimensional floating object with six degrees of freedom, so the equations for the ship dynamics written in Section 2.4.2 need to be extended.

First, let us define the vectors:

$$\boldsymbol{G} = \begin{pmatrix} x_G \\ y_G \\ z_G \end{pmatrix}, \quad \boldsymbol{u}_G = \begin{pmatrix} u_G \\ v_G \\ w_G \end{pmatrix}, \quad \boldsymbol{\varphi} = \begin{pmatrix} \varphi_x \\ \varphi_y \\ \varphi_z \end{pmatrix}, \quad \boldsymbol{F} = \begin{pmatrix} F_x \\ F_y \\ F_z \end{pmatrix}, \quad \boldsymbol{\tau} = \begin{pmatrix} \tau_x \\ \tau_y \\ \tau_z \end{pmatrix}.$$

$\boldsymbol{G}$ is the position of the center of mass relative to the inertial frame of reference. The others are relative to the fixed-body frame of reference: $\boldsymbol{u}_G$ holds the ship velocities so that u_G is the surge motion, v_G is the sway motion, w_G is the heave motion; they change when subject to the force $\boldsymbol{F}$. The orientation $\boldsymbol{\varphi}$ is relative to the $x'y'z'$ axes and change when the body is subject to the torque $\boldsymbol{\tau}$, causing roll, pitch and yaw motion. A sketch of the problem configuration is shown in Figure 13. The system of equation that describes the translation and rotation of the vessel is the following:

$$m_s \dot{\boldsymbol{u}}_G^{n+1} + \dot{\boldsymbol{\varphi}}^n \times (m_s \boldsymbol{u}_G^n) = \boldsymbol{F}^n, \tag{34a}$$

$$\boldsymbol{I}_s \ddot{\boldsymbol{\varphi}}^{n+1} + \dot{\boldsymbol{\varphi}}^n \times (\boldsymbol{I}_s \dot{\boldsymbol{\varphi}}^n) = \boldsymbol{\tau}^n. \tag{34b}$$

Here, $\dot{\boldsymbol{u}}$ is the linear acceleration, $\dot{\boldsymbol{\varphi}}$ is the angular velocity and $\ddot{\boldsymbol{\varphi}}$ is the angular acceleration. $\boldsymbol{I}_s$ is the inertia tensor computed in the body-fixed frame of reference (so it is constant during the simulation):

$$\boldsymbol{I}_s = \begin{bmatrix} I_x & -I_{xy} & -I_{xz} \\ -I_{yx} & I_y & -I_{yz} \\ -I_{zx} & -I_{zy} & I_z \end{bmatrix},$$

whose components are the moments and products of inertia:

$$\begin{aligned} I_x &= \sum_s m_{s,s}(y'^2_s + z'^2_s) & \qquad I_{xy} = I_{yx} &= \sum_s m_{s,s}\, x'_s\, y'_s, \\ I_y &= \sum_s m_{s,s}(x'^2_s + z'^2_s) & I_{xz} = I_{zx} &= \sum_s m_{s,s}\, x'_s\, z'_s, \\ I_z &= \sum_s m_{s,s}(x'^2_s + y'^2_s) & I_{yz} = I_{zy} &= \sum_s m_{s,s}\, y'_s\, z'_s. \end{aligned} \tag{35}$$

In analogy with Section 2.4.2, the force $\boldsymbol{F}$ is generated by gravity and the hydrostatic pressure acting on the hull. The pressure force is always orthogonal to the hull, so a normal vector is computed in each subcell relevant for the ship; to do so, it is possible to leverage the parametric representation of ship (see Figure 6): two vectors are drawn from the subcell center to the vertices of the polygon surrounding the center. Further on, we apply a normalized orthogonal vector $\hat{n}_s = \{\hat{n}_{x,s}, \hat{n}_{y,s}, \hat{n}_{z,s}\}$ resulting from the cross product of these two vectors. The forces are computed in a frame of reference parallel to the inertial one but centered in $\boldsymbol{G}$ (we mark them with a tilde):

$$\begin{aligned} \tilde{F}_x &= \sum_s \tilde{F}_{x,s} & \quad \text{with} \quad \tilde{F}_{x,s} &= \rho g \, \max(0, \eta_s - l_s) \frac{\Delta x_s \Delta y_s}{||\hat{n}_{z,s}||} \hat{n}_{x,s}, \\ \tilde{F}_y &= \sum_s \tilde{F}_{y,s} & \quad \text{with} \quad \tilde{F}_{y,s} &= \rho g \, \max(0, \eta_s - l_s) \frac{\Delta x_s \Delta y_s}{||\hat{n}_{z,s}||} \hat{n}_{y,s}, \\ \tilde{F}_z &= \sum_s \tilde{F}_{z,s} - mg & \quad \text{with} \quad \tilde{F}_{z,s} &= \rho g \, \max(0, \eta_s - l_s) \frac{\Delta x_s \Delta y_s}{||\hat{n}_{z,s}||} \hat{n}_{z,s}. \end{aligned} \tag{36}$$

The fraction $\frac{\Delta x_s \Delta y_s}{||\hat{n}_{z,s}||}$ is the approximation of the hull area included in the subcell: the subcell area $\Delta x_s \Delta y_s$ is increased though a division with the inclination of the hull with respect to the horizontal plane, represented by the magnitude of $\hat{n}_{z,s}$, which is $0 < ||\hat{n}_{z,s}|| \leq 1$ ($= 1$ when the piece of the vessel hull in s is horizontal). The torques are the products of these forces on the hull with the distances to the axes (which are centered in $\boldsymbol{G}$), following the right hand rule:

$$\begin{aligned}
\tilde{\tau}_x &= \sum_s \left[\tilde{F}_{y,s}(z_G - l_s) + \tilde{F}_{z,s}(y_s - y_G)\right], \\
\tilde{\tau}_y &= \sum_s \left[\tilde{F}_{z,s}(x_G - x_s) + \tilde{F}_{x,s}(l_s - z_G)\right], \\
\tilde{\tau}_z &= \sum_s \left[\tilde{F}_{x,s}(y_G - y_s) + \tilde{F}_{y,s}(x_s - x_G)\right].
\end{aligned} \tag{37}$$

In order to relate the forces and torques to the body-fixed frame of reference the rotation matrix $\boldsymbol{R}$ is applied:

$$\boldsymbol{R} = \begin{bmatrix} \cos(\varphi_z) & -\sin(\varphi_z) & 0 \\ \sin(\varphi_z) & \cos(\varphi_z) & 0 \\ 0 & 0 & 1 \end{bmatrix} \begin{bmatrix} \cos(\varphi_y) & 0 & \sin(\varphi_y) \\ 0 & 1 & 0 \\ -\sin(\varphi_y) & 0 & \cos(\varphi_y) \end{bmatrix} \begin{bmatrix} 1 & 0 & 0 \\ 0 & \cos(\varphi_x) & -\sin(\varphi_x) \\ 0 & \sin(\varphi_x) & \cos(\varphi_x) \end{bmatrix}. \tag{38}$$

So that:

$$\begin{aligned}
\boldsymbol{F} &= \boldsymbol{R}^T \tilde{\boldsymbol{F}}, \\
\boldsymbol{\tau} &= \boldsymbol{R}^T \tilde{\boldsymbol{\tau}}.
\end{aligned} \tag{39}$$

It is now possible to solve system (34). In explicit form:

$$\begin{cases}
\dot{u}^{n+1} - v^n \dot{\varphi}_z^n + w^n \dot{\varphi}_y^n = \frac{F_x^n}{m} \\
\dot{v}^{n+1} - w^n \dot{\varphi}_x^n + u^n \dot{\varphi}_z^n = \frac{F_y^n}{m} \\
\dot{w}^{n+1} - u^n \dot{\varphi}_y^n + v^n \dot{\varphi}_x^n = \frac{F_z^n}{m} \\
I_x \ddot{\varphi}_x^{n+1} + (I_z - I_y)\dot{\varphi}_y^n \dot{\varphi}_z^n - (\ddot{\varphi}_z^{n+1} + \dot{\varphi}_x^n \dot{\varphi}_y^n) I_{xz} + (\dot{\varphi}_y^2 - \dot{\varphi}_z^2)^n I_{yz} + (\dot{\varphi}_x^n \dot{\varphi}_z^n - \ddot{\varphi}_y^{n+1}) I_{xy} = \tau_x^n \\
I_y \ddot{\varphi}_y^{n+1} + (I_x - I_z)\dot{\varphi}_z^n \dot{\varphi}_x^n - (\ddot{\varphi}_x^{n+1} + \dot{\varphi}_y^n \dot{\varphi}_z^n) I_{yx} + (\dot{\varphi}_z^2 - \dot{\varphi}_x^2)^n I_{zx} + (\dot{\varphi}_y^n \dot{\varphi}_x^n - \ddot{\varphi}_z^{n+1}) I_{yz} = \tau_y^n \\
I_z \ddot{\varphi}_z^{n+1} + (I_y - I_x)\dot{\varphi}_x^n \dot{\varphi}_y^n - (\ddot{\varphi}_y^{n+1} + \dot{\varphi}_z^n \dot{\varphi}_x^n) I_{zy} + (\dot{\varphi}_x^2 - \dot{\varphi}_y^2)^n I_{xy} + (\dot{\varphi}_z^n \dot{\varphi}_y^n - \ddot{\varphi}_x^{n+1}) I_{zx} = \tau_z^n
\end{cases}. \tag{40}$$

The equations for the conservation of the angular momentum are coupled, so the matrix form is solved to get the unknown $\ddot{\boldsymbol{\varphi}}^{n+1}$:

$$\begin{pmatrix} I_x & -I_{xy} & -I_{xz} \\ -I_{yx} & I_y & -I_{yz} \\ -I_{zx} & -I_{zy} & I_z \end{pmatrix} \begin{pmatrix} \ddot{\varphi}_x^{n+1} \\ \ddot{\varphi}_y^{n+1} \\ \ddot{\varphi}_z^{n+1} \end{pmatrix} = \begin{pmatrix} \tau_x^n - (I_z - I_y)\dot{\varphi}_y^n \dot{\varphi}_z^n + \dot{\varphi}_x^n \dot{\varphi}_y^n I_{xz} - (\dot{\varphi}_y^2 - \dot{\varphi}_z^2)^n I_{yz} - \dot{\varphi}_x^n \dot{\varphi}_z^n I_{xy} \\ \tau_y^n - (I_x - I_z)\dot{\varphi}_z^n \dot{\varphi}_x^n + \dot{\varphi}_y^n \dot{\varphi}_z^n I_{yx} - (\dot{\varphi}_z^2 - \dot{\varphi}_x^2)^n I_{zx} - \dot{\varphi}_y^n \dot{\varphi}_x^n I_{yz} \\ \tau_z^n - (I_y - I_x)\dot{\varphi}_x^n \dot{\varphi}_y^n + \dot{\varphi}_z^n \dot{\varphi}_x^n I_{zy} - (\dot{\varphi}_x^2 - \dot{\varphi}_y^2)^n I_{xy} - \dot{\varphi}_z^n \dot{\varphi}_y^n I_{zx} \end{pmatrix}. \tag{41}$$

Once the solution for $\dot{\boldsymbol{u}}^{n+1}$ and $\ddot{\boldsymbol{\varphi}}^{n+1}$ is found, the position, orientation and the velocities are updated with a second order Taylor method:

$$\begin{aligned}
\boldsymbol{u}^{n+1} &= \boldsymbol{u}^n + \Delta t\, \dot{\boldsymbol{u}}^{n+1}, \\
\boldsymbol{R}^T \boldsymbol{G}^{n+1} &= \boldsymbol{R}^T \boldsymbol{G}^n + \Delta t\, \boldsymbol{u}^n + \frac{\Delta t^2}{2} \dot{\boldsymbol{u}}^{n+1}, \\
\dot{\boldsymbol{\varphi}}^{n+1} &= \dot{\boldsymbol{\varphi}}^n + \Delta t\, \ddot{\boldsymbol{\varphi}}^{n+1}, \\
\boldsymbol{\varphi}^{n+1} &= \boldsymbol{\varphi}^n + \Delta t\, \dot{\boldsymbol{\varphi}}^n + \frac{\Delta t^2}{2} \ddot{\boldsymbol{\varphi}}^{n+1}.
\end{aligned} \tag{42}$$

Figure 14 shows a typical output of the ship dynamics based on the model presented in this section in combination with the 3D hydrodynamics shown in the subsequent section. The figure also highlights the freedom in the definition of the shape of the hull, that is, it is possible to simulate the motion of reasonably complex objects.

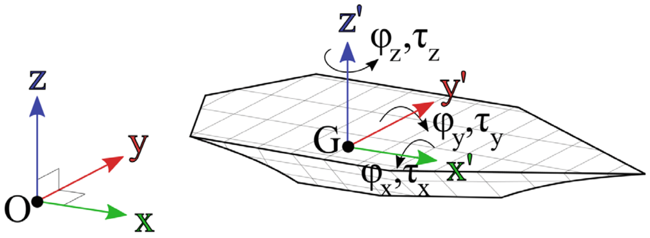

FIGURE 13 General $2D_{xy}$/3D scheme of the ship motion problem [Colour figure can be viewed at wileyonlinelibrary.com]

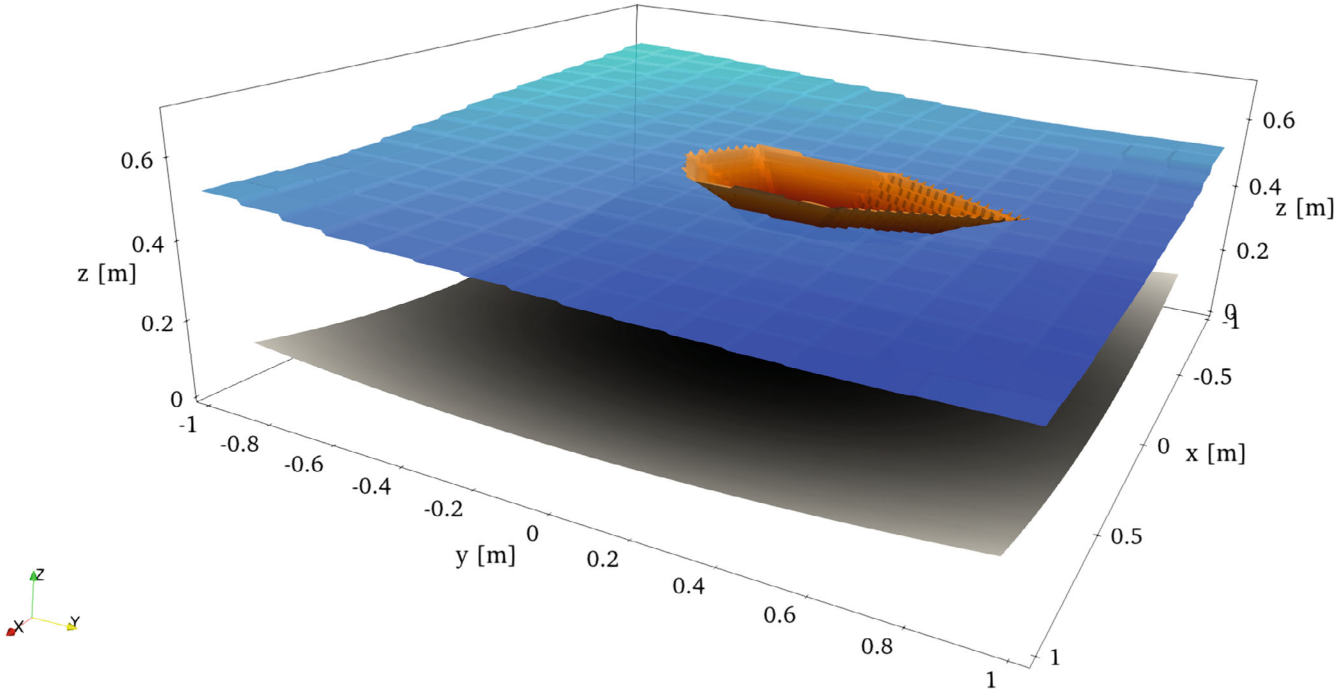

FIGURE 14 Representation of a ship floating on water in a 3D simulation [Colour figure can be viewed at wileyonlinelibrary.com]

2.7 | 3D model

The 3D model is a direct extension of the concepts explained in Section 2.5. The mass equation has two differences of fluxes for the x and y directions, and each flux is an integral over the vertical of the linear momentum. The momentum equations have all the advective terms, the pressure gradients and the viscosity along the vertical. As explained for the $2D_{xz}$ model, the system is initially written in continuous form with primitive variables. The discretized form involving the fluxes q_x and q_y is obtained after integration of the momentum equations along the vertical.

$$\frac{\partial}{\partial t}\left[H(\eta)\right] + \frac{\partial}{\partial x}\left[\int_b^\eta u(x,y,z,t)dz\right] + \frac{\partial}{\partial y}\left[\int_b^\eta v(x,y,z,t)dz\right] = 0, \tag{43a}$$

$$\frac{\partial u}{\partial t} + \frac{\partial\,(uu)}{\partial x} + \frac{\partial\,(uv)}{\partial y} + \frac{\partial\,(uw)}{\partial z} + g\frac{\partial \eta}{\partial x} = +\frac{\partial}{\partial z}\left(\nu\frac{\partial u}{\partial z}\right), \tag{43b}$$

$$\frac{\partial v}{\partial t} + \frac{\partial\,(vu)}{\partial x} + \frac{\partial\,(vv)}{\partial y} + \frac{\partial\,(vw)}{\partial z} + g\frac{\partial \eta}{\partial y} = +\frac{\partial}{\partial z}\left(\nu\frac{\partial v}{\partial z}\right), \tag{43c}$$

$$\frac{\partial u}{\partial x} + \frac{\partial v}{\partial y} + \frac{\partial w}{\partial z} = 0. \tag{43d}$$

The boundary conditions for the wind stress and the bottom friction act in the cells with a dry/wet or wet/air interface and read:

$$\begin{cases} \nu \dfrac{\partial u}{\partial z} = \gamma_T \left(u^a - u^s\right) & \text{at the free surface} \\ \nu \dfrac{\partial v}{\partial z} = \gamma_T \left(v^a - v^s\right) & \text{at the free surface} \\ \nu \dfrac{\partial u}{\partial z} = \gamma_B u^b & \text{at the bottom} \\ \nu \dfrac{\partial v}{\partial z} = \gamma_B v^b & \text{at the bottom} \end{cases} \tag{44}$$

with γ_T and γ_B defined as

$$\gamma_T = C_d \frac{\rho_a}{\rho} \sqrt{(u^a)^2 + (v^a)^2}, \qquad \gamma_B = \frac{g\sqrt{(u^b)^2 + (v^b)^2}}{k_s^2 R_h^{1/3}}. \tag{45}$$

The integrals are approximated similarly to Equation (23), but, due to the use of a staggered grid, in 2D$_{xy}$/3D they are calculated at every interface along x and y (in total $(I_{\max} + 1)J_{\max} + (J_{\max} + 1)I_{\max}$ times):

$$\int_b^\eta u dz \approx \sum_k \Delta z_{i+\frac{1}{2},j,k} u_{i+\frac{1}{2},j,k}, \qquad \int_b^\eta v dz \approx \sum_k \Delta z_{i+\frac{1}{2},j,k} v_{i,j+\frac{1}{2},k}, \qquad k = 1, 2, \ldots, K_{\max}, \tag{46}$$

with the vertical spacings $\Delta z_{i+\frac{1}{2},j,k} = \Delta z$ and $\Delta z_{i,j+\frac{1}{2},k} = \Delta z$, where the first and last layer are adjusted so that

$$\begin{aligned} \sum_k \Delta z_{i+\frac{1}{2},j,k} &= \max\left(0, \min\left(\eta_{i+\frac{1}{2},j} - b_{i+\frac{1}{2},j}, l_{i+\frac{1}{2},j} - b_{i+\frac{1}{2},j}\right)\right), \\ \sum_k \Delta z_{i,j+\frac{1}{2},k} &= \max\left(0, \min\left(\eta_{i,j+\frac{1}{2}} - b_{i,j+\frac{1}{2}}, l_{i,j+\frac{1}{2}} - b_{i,j+\frac{1}{2}}\right)\right). \end{aligned} \tag{47}$$

Consequently, it is possible to identify the partially wet cells along the vertical, marked with the start and end indeces $m_{i+\frac{1}{2},j}$, $m_{i,j+\frac{1}{2}}$, $M^n_{i+\frac{1}{2},j}$, $M^n_{i,j+\frac{1}{2}}$. They will impose the dimension of the arrays along the vertical.

The advective terms $\partial(q_x u)/\partial x$ and $\partial(q_y v)/\partial y$ are discretized with the numerical fluxes presented in Section 2.4.3. The advective term $\partial(q_x w)/\partial z$ is the same as in Equation (25), with the addition of the missing j index. The new mixed terms $\partial(q_x v)/\partial y$, $\partial(q_y u)/\partial x$ and $\partial(q_y w)/\partial z$ follow again the central scheme:

$$\frac{\partial\left(q_x v\right)}{\partial y} \approx \frac{1}{\Delta y}\left(\frac{(q_x)^n_{i+\frac{1}{2},j+1,k} + (q_x)^n_{i+\frac{1}{2},j,k}}{2}\right)\left(\frac{v^n_{i+1,j+\frac{1}{2},k} + v^n_{i,j+\frac{1}{2},k}}{2}\right) - \frac{1}{\Delta y}\left(\frac{(q_x)^n_{i+\frac{1}{2},j,k} + (q_x)^n_{i+\frac{1}{2},j-1,k}}{2}\right)\left(\frac{v^n_{i+1,j-\frac{1}{2},k} + v^n_{i,j-\frac{1}{2},k}}{2}\right), \tag{48}$$

$$\frac{\partial\left(q_y u\right)}{\partial x} \approx \frac{1}{\Delta x}\left(\frac{\left(q_y\right)^n_{i+1,j+\frac{1}{2},k} + \left(q_y\right)^n_{i,j+\frac{1}{2},k}}{2}\right)\left(\frac{u^n_{i+\frac{1}{2},j+1,k} + u^n_{i+\frac{1}{2},j,k}}{2}\right) - \frac{1}{\Delta x}\left(\frac{\left(q_y\right)^n_{i,j+\frac{1}{2},k} + \left(q_y\right)^n_{i-1,j+\frac{1}{2},k}}{2}\right)\left(\frac{u^n_{i-\frac{1}{2},j+1,k} + u^n_{i-\frac{1}{2},j,k}}{2}\right), \tag{49}$$

$$\frac{\partial\left(q_y w\right)}{\partial z} \approx \frac{1}{\Delta z_y}\left(\frac{\left(q_y\right)^n_{i,j+\frac{1}{2},k+1} + \left(q_y\right)^n_{i,j+\frac{1}{2},k}}{2}\right)\left(\frac{w^n_{i,j+1,k+\frac{1}{2}} + w^n_{i,j,k+\frac{1}{2}}}{2}\right) - \frac{1}{\Delta z_y}\left(\frac{\left(q_y\right)^n_{i,j+\frac{1}{2},k} + \left(q_y\right)^n_{i,j+\frac{1}{2},k-1}}{2}\right)\left(\frac{w^n_{i,j+1,k-\frac{1}{2}} + w^n_{i,j,k-\frac{1}{2}}}{2}\right). \tag{50}$$

The time step limitation is set according to a CFL-type condition as follows:

$$\Delta t = \min\left(\Delta t_{\max}\,, \frac{\text{CFL}}{2\left(\frac{|u|_{\max}}{\Delta x} + \frac{|v|_{\max}}{\Delta y}\right) + c}\right) \qquad \text{with CFL} = 0.9. \tag{51}$$

The viscous term along x is discretized exactly like in Equation (27), but adding a j index everywhere; in the y direction:

$$\frac{\partial}{\partial z}\left(\Delta z \nu \frac{\partial v}{\partial z}\right) \approx \frac{1}{\Delta z^{n}_{i,j+\frac{1}{2},k}}\left[\nu^{n+1}_{i,j+\frac{1}{2},k+\frac{1}{2}}\left(v^{n+1}_{i,j+\frac{1}{2},k+1}-v^{n+1}_{i,j+\frac{1}{2},k}\right)-\nu^{n+1}_{i,j+\frac{1}{2},k-\frac{1}{2}}\left(v^{n+1}_{i,j+\frac{1}{2},k}-v^{n+1}_{i,j+\frac{1}{2},k-1}\right)\right]. \tag{52}$$

Defining the discrete volume in a cell as $V^n_{i,j} = \Delta x \Delta y H^n_{i,j}$ and using the shorthand notation $V^n_{i,j} = V(\eta^n_{i,j}, \mathbf{G}^n, \boldsymbol{\varphi}^n)$ the discretized form of system (43) is:

$$V^{n+1}_{i,j} = V^n_{i,j} - \Delta y \Delta t\left[\left(\boldsymbol{\Delta Z}^T\boldsymbol{U}\right)^{n+\theta}_{i+\frac{1}{2},j} - \left(\boldsymbol{\Delta Z}^T\boldsymbol{U}\right)^{n+\theta}_{i-\frac{1}{2},j}\right] - \Delta x \Delta t\left[\left(\boldsymbol{\Delta Z}^T\boldsymbol{V}\right)^{n+\theta}_{i,j+\frac{1}{2}} - \left(\boldsymbol{\Delta Z}^T\boldsymbol{V}\right)^{n+\theta}_{i,j-\frac{1}{2}}\right], \tag{53a}$$

$$\boldsymbol{A}^n_{i+\frac{1}{2},j}\boldsymbol{U}^{n+1}_{i+\frac{1}{2},j} = \boldsymbol{G}^n_{i+\frac{1}{2},j} - g\frac{\Delta t}{\Delta x}\left(\eta^{n+\theta}_{i+1,j} - \eta^{n+\theta}_{i,j}\right)\boldsymbol{\Delta Z}^2_{i+\frac{1}{2},j}, \tag{53b}$$

$$\boldsymbol{A}^n_{i,j+\frac{1}{2}}\boldsymbol{V}^{n+1}_{i,j+\frac{1}{2}} = \boldsymbol{G}^n_{i,j+\frac{1}{2}} - g\frac{\Delta t}{\Delta y}\left(\eta^{n+\theta}_{i,j+1} - \eta^{n+\theta}_{i,j}\right)\boldsymbol{\Delta Z}^2_{i,j+\frac{1}{2}}. \tag{53c}$$

For what concerns the momentum along x, the general definitions of the vectors are the same of (29) and (30), but now they must be computed for every j; for the vectors along y one simply substitutes all the u with v. There is only one single difference in the definition of $\boldsymbol{A}^n$, due to the fact that in 3D there is no more a term γq^{n+1}: d_k changes to $d_k = \Delta z_k^2$, for $k = m, m+1, \dots, M$.

The substitution of the momentum equation in the mass equation leads to:

$$\begin{aligned} V^{n+1}_{i,j} &- g\Delta y\frac{\Delta t^2}{\Delta x}\left\{\left(\theta\boldsymbol{\Delta} Z^T\boldsymbol{A}^{-1}\boldsymbol{\Delta Z^2}\right)^n_{i+\frac{1}{2},j}\left[(\theta\eta)^{n+1}_{i+1,j} - (\theta\eta)^{n+1}_{i,j}\right] - \left(\theta\boldsymbol{\Delta} Z^T\boldsymbol{A}^{-1}\boldsymbol{\Delta Z^2}\right)^n_{i-\frac{1}{2},j}\left[(\theta\eta)^{n+1}_{i,j} - (\theta\eta)^{n+1}_{i-1,j}\right]\right\} \\ &- g\Delta x\frac{\Delta t^2}{\Delta y}\left\{\left(\theta\boldsymbol{\Delta} Z^T\boldsymbol{A}^{-1}\boldsymbol{\Delta Z^2}\right)^n_{i,j+\frac{1}{2}}\left[(\theta\eta)^{n+1}_{i,j+1} - (\theta\eta)^{n+1}_{i,j}\right] - \left(\theta\boldsymbol{\Delta} Z^T\boldsymbol{A}^{-1}\boldsymbol{\Delta Z^2}\right)^n_{i,j-\frac{1}{2}}\left[(\theta\eta)^{n+1}_{i,j} - (\theta\eta)^{n+1}_{i,j-1}\right]\right\} = r^n_{i,j}, \end{aligned} \tag{54}$$

with

$$\begin{aligned} r^n_{i,j} = V^n_{i,j} &- \Delta y\Delta t\left[\left(\theta\boldsymbol{\Delta} Z^T\boldsymbol{A}^{-1}\boldsymbol{G}\right)^n_{i+\frac{1}{2},j} - \left(\theta\boldsymbol{\Delta} Z^T\boldsymbol{A}^{-1}\boldsymbol{G}\right)^n_{i-\frac{1}{2},j}\right] - \Delta x\Delta t\left[\left(\theta\boldsymbol{\Delta} Z^T\boldsymbol{A}^{-1}\boldsymbol{G}\right)^n_{i,j+\frac{1}{2}} - \left(\theta\boldsymbol{\Delta} Z^T\boldsymbol{A}^{-1}\boldsymbol{G}\right)^n_{i,j-\frac{1}{2}}\right] \\ &- \Delta y\Delta t\left\{\left[(1-\theta)\boldsymbol{\Delta} Z^T\boldsymbol{U}\right]^n_{i+\frac{1}{2},j} - \left[(1-\theta)\boldsymbol{\Delta} Z^T\boldsymbol{U}\right]^n_{i-\frac{1}{2},j}\right\} - \Delta x\Delta t\left\{\left[(1-\theta)\boldsymbol{\Delta} Z^T\boldsymbol{V}\right]^n_{i,j+\frac{1}{2}} - \left[(1-\theta)\boldsymbol{\Delta} Z^T\boldsymbol{V}\right]^n_{i,j-\frac{1}{2}}\right\} \\ &+ g\Delta y\frac{\Delta t^2}{\Delta x}\left\{\left(\theta\boldsymbol{\Delta} Z^T\boldsymbol{A}^{-1}\boldsymbol{\Delta Z^2}\right)^n_{i+\frac{1}{2},j}\left[((1-\theta)\,\eta)^n_{i+1,j} - ((1-\theta)\,\eta)^n_{i,j}\right]\right. \\ &\quad\left. - \left(\theta\boldsymbol{\Delta} Z^T\boldsymbol{A}^{-1}\boldsymbol{\Delta Z^2}\right)^n_{i-\frac{1}{2},j}\left[((1-\theta)\,\eta)^n_{i,j} - ((1-\theta)\,\eta)^n_{i-1,j}\right]\right\} \\ &+ g\Delta x\frac{\Delta t^2}{\Delta y}\left\{\left(\theta\boldsymbol{\Delta} Z^T\boldsymbol{A}^{-1}\boldsymbol{\Delta Z^2}\right)^n_{i,j+\frac{1}{2}}\left[((1-\theta)\,\eta)^n_{i,j+1} - ((1-\theta)\,\eta)^n_{i,j}\right]\right. \\ &\quad\left. - \left(\theta\boldsymbol{\Delta} Z^T\boldsymbol{A}^{-1}\boldsymbol{\Delta Z^2}\right)^n_{i,j-\frac{1}{2}}\left[((1-\theta)\,\eta)^n_{i,j} - ((1-\theta)\,\eta)^n_{i,j-1}\right]\right\}. \end{aligned} \tag{55}$$

The resulting mildly nonlinear pressure system is again solved with the nested Newton method detailed in References 43 and 44. Again the Thomas algorithm is used for computing all terms of the type $\boldsymbol{A}^{-1}\boldsymbol{\Delta Z}^2$ and $\boldsymbol{A}^{-1}\boldsymbol{G}$. The solution of the five-diagonal system is obtained applying a matrix-free conjugate gradient method; with $\boldsymbol{\eta}^{n+1}$, the horizontal velocities at the new time step are found from the momentum equations. Finally, the vertical velocities are computed from the incompressibility constraint. Starting from the bottom with $w^{n+1}_{i,j,m-\frac{1}{2}} = 0$, the others are obtained by

$$w^{n+1}_{i,j,k+\frac{1}{2}} = w^{n+1}_{i,j,k-\frac{1}{2}} - \frac{\Delta z^n_{i+\frac{1}{2},j,k}u^{n+1}_{i+\frac{1}{2},j,k} - \Delta z^n_{i-\frac{1}{2},j,k}u^{n+1}_{i-\frac{1}{2},j,k}}{\Delta x} - \frac{\Delta z^n_{i,j+\frac{1}{2},k}v^{n+1}_{i,j+\frac{1}{2},k} - \Delta z^n_{i,j-\frac{1}{2},k}v^{n+1}_{i,j-\frac{1}{2},k}}{\Delta y}, \quad k = m_i, m_i+1, \dots, M^n_i - 1. \tag{56}$$

The 3D model automatically reduces to all the previously presented models, setting appropriately $K_{\max} = 1$ and/or $J_{\max} = 1$.

3 | NUMERICAL RESULTS

In this section, we verify the model features and capabilities applying it to a selection of test cases. At the beginning, we verify the model applied for flows without floating objects and compare the results to available exact solutions. In the following, we study the response of a ship in various simple fluid-structure interaction situations concentrating on the vertical degree of freedom (heaving). For a basic consistency-check of the method with elementary physics, the main requirement is the straightforward test that when the ship is in static equilibrium in a still water body, its position in time should not change, which checks if the method is well-balanced.[54,55] Having checked this seemingly trivial property, we proceeded to verify the heaving motion with a floating body set in an unbalanced position. The use of a simplified hull geometry allows to obtain an analytical solution of the damped-harmonic oscillator equation for the body motion, which is compared to the results obtained with the numerical method presented in this article. All the following results are obtained applying the implementation of the 3D model in form of a Fortran code and we visualized the results using ParaView. As was mentioned in Sections 2.5 and 2.7, with the complete model we can get 1D or 2D simulations with an appropriate choice of the cells number in each direction. Each test case is useful to highlight and verify specific features of the model:

- Dam-break problems over wet and dry bed (Section 3.1): shock capturing, wetting and drying, importance of the momentum conservative discretization,
- Uniform flow (Section 3.2): Dirichlet and Neumann boundary conditions, bottom friction,
- Oscillations in a lake (Section 3.3): wetting and drying, nontrivial bottom with subgrid, numerical dissipation,
- Return to equilibrium in deep water (Section 3.4): heaving response and waves generation,
- Return to equilibrium in shallow water (Section 3.5): effects of the water depth on the heaving response and the waves generation,
- Heaving due to incoming waves (Section 3.6): response to external regular wave field.

Throughout this section we make use of the SI system of units.

3.1 | Dam-break problems over wet and dry bed

The first validation is a classical test problem in CFD, namely the so-called Riemann problem or dambreak problem for shallow water flows. We consider two cases here, one dambreak over wet bed and another one over dry bed. In both cases the bottom is flat ($b = 0$). In order to properly validate the 2Dxz model, we carry out each simulation with a single layer $\Delta z > H$ and with a number of z-layers of maximum size of $\Delta z_k = 0.1$, apart from the uppermost layer, whose size is dynamically adjusted in order to fit the free surface. Since the vertical viscosity coefficient is set to $\nu = 0$, the vertical velocity profile is constant and therefore the 1D model and the 2Dxz model must produce the same results.

Dambreak over wet bed

The initial condition of the first Riemann problem consists in still water over flat bottom, with left water depth $H_L = 2$ and right water depth $H_R = 1$. A constant time step of $\Delta t = 1 \cdot 10^{-3}$ is used on a uniform Cartesian mesh composed of 100 cells in x direction. No-flux boundary conditions are applied on the left and right boundaries. In the left panel of Figure 15 the obtained numerical solution is compared against the exact solution provided by Stoker,[56] and also available in the textbook of Toro.[57] The numerical results obtained with the mass and momentum conservative semi-implicit scheme agree well with the reference solution, capturing both the wave heights and the wave propagation speeds in a correct manner. We also observe that the solution obtained with the 1D model and the 2Dxz model coincide, as expected.

Dam-break over dry bed

In the initial condition of the second Riemann problem the downstream side is dry. The comparison is made with Ritter's solution,[58] which is formulated for a frictionless wide horizontal channel. Its biggest merit is simplicity, so

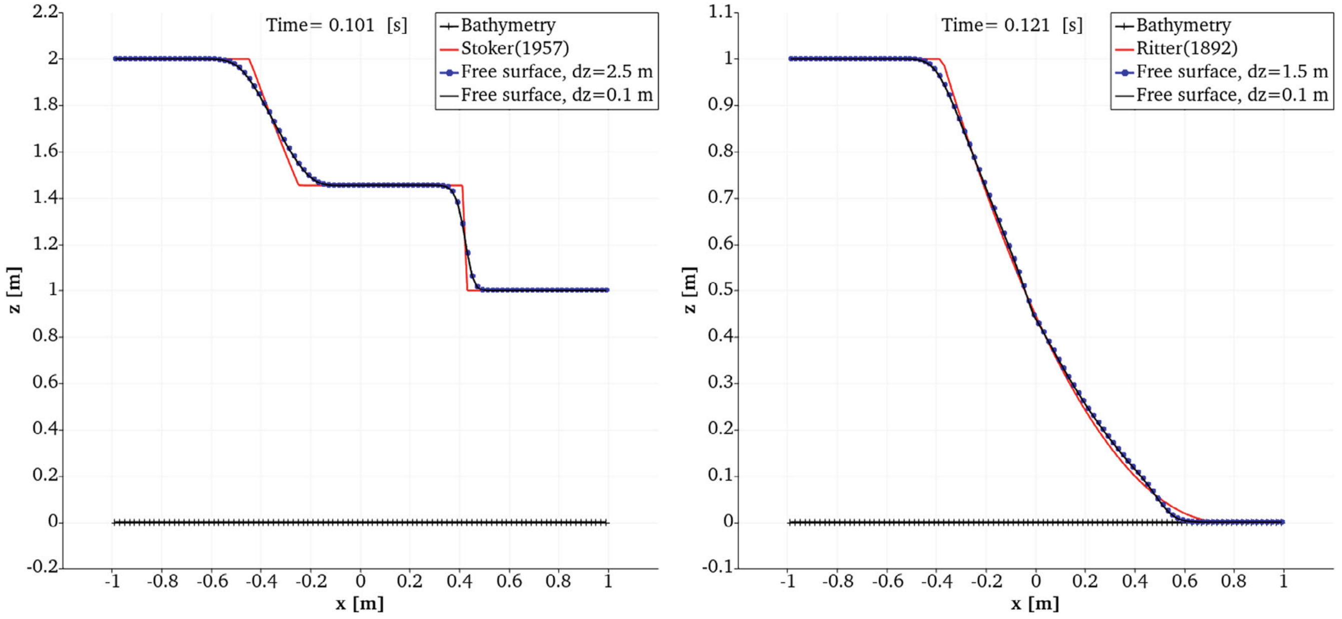

FIGURE 15 Two dam break problems. Dambreak over wet bed (left): Comparison of the new momentum conservative semi-implicit scheme with the analytical solution of Stoker (1957); comparison between the 2Dxz model with maximum layer size $\Delta z = 0.1$ and the 1D model with only one layer of maximum size $\Delta z = 2.5$. Dambreak over dry bed (right): Comparison of the new momentum conservative semi-implicit scheme with the analytical solution of Ritter (1892); comparison between the 2Dxz model of maximum layer size $\Delta z = 0.1$ and the 1D model with only one layer of maximum size $\Delta z = 1.5$. [Colour figure can be viewed at wileyonlinelibrary.com]

it is a quick test to see if the wet/dry transition is treated appropriately. However, it is not in good agreement with experimental data because it does not consider friction, turbulence, vertical acceleration and nonhydrostatic pressure, see Reference 59. The exact solution of the Riemann problem can be found in Reference 58, or in the textbook.[57] In the numerical simulation the boundary conditions are no-flux, the Strickler coefficient is set to $k_s = 100$ so that bottom friction can be essentially neglected, the initial location of the dam is in $x_0 = 0$, the initial water heights on the left and on the right of the dam are $H_L = 1$ and $H_R = 0$, respectively, the initial velocity is zero in the entire domain, a constant time step of $\Delta t = 1 \cdot 10^{-3}$ is used and the number of cells is set to $I_{\max} = 100$. The results are shown in the right panel of Figure 15. There is a good agreement between the numerical results and the analytical solution. We highlight that the numerical solution is a rarefaction wave thanks to the conservative discretization of the mass and momentum conservation equations, see also References 50 and 60 for the importance of momentum conservation in rapidly varied flows. For an alternative nonconservative discretization of the shallow water equations, unphysical solutions are obtained. Again, the 1D model and the 2Dxz model agree perfectly well with each other, as expected.

3.2 | Uniform flow

With the introduction of bottom friction in the model, it is possible to compute a numerical test case of the uniform flow in an open channel, proving the model ability to maintain it. In a uniform flow, both time derivative and the advection term vanish, so there exist a characteristic equilibrium between the pressure gradient and the friction term. The conditions for this flow to realize are that the inflow discharge remains constant in time and that the shape of the channel does not change in the direction of the flow. These are essentially never met in a real-world scenario; nonetheless, this flow condition is of great interest as a reference point and also because it can give insights about a river free-surface elevation as a function of flow velocity and average bottom slope. The equation that governs the flow is the Gauckler–Manning–Strickler formula:[61,62]

$$u = k_s\, R_h^{\frac{2}{3}}\, s^{\frac{1}{2}}, \tag{57}$$

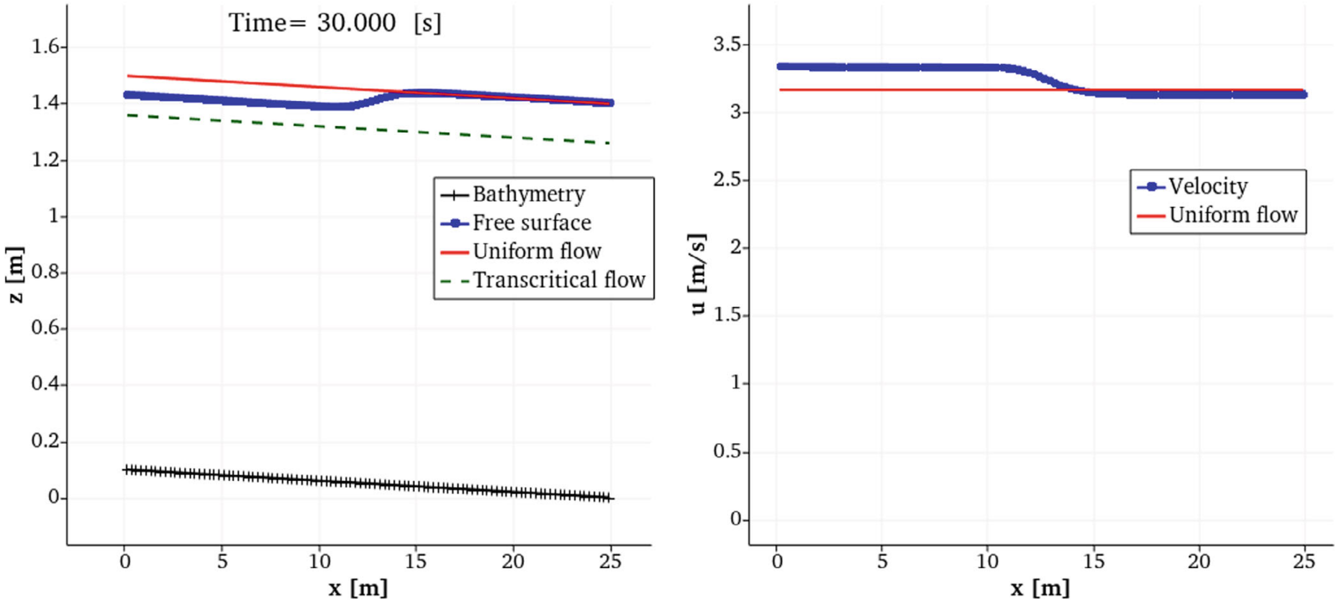

FIGURE 16 Numerical simulation of the uniform flow, starting from nonuniform flow conditions. At this timestep, the transition from initial to uniform conditions is still in progress, with a wave ascending from east to west. [Colour figure can be viewed at wileyonlinelibrary.com]

where s is the constant bottom slope $s = -b_x$. Under the assumption of wide and rectangular channel, an explicit formula for the uniform water depth H_u can be derived:

$$H_u = \left(\frac{q}{k_s \sqrt{s}} \right)^{\frac{3}{5}}. \tag{58}$$

Another parameter of interest is the critical water depth H_c, the depth of the transcritical flow at a given discharge:

$$H_c = \sqrt[3]{\frac{q^2}{g}}. \tag{59}$$

With the background theory set in place, a simulation of a subcritical flow is presented. The initial conditions are a constant flux and a water height lower than the uniform one. On the west side, the Neumann boundary condition is constant in time and it is the initial water discharge q_0, on the east side the Dirichlet boundary condition imposes the water depth H_u. The parameters of the chosen computational test problem are $q_0 = 4.42$ for the inflow discharge, $H_0 = 1.27$ the initial water height, $H_c = 1.26$ the critical depth, $H_u = 1.4$ the uniform flow depth, $k_s = 40$ the Strickler coefficient, $s = 4 \cdot 10^{-3}$ the constant bottom slope and $I_{\max} = 100$ the number of cells. The results are shown in Figure 16, at time $t = 30$ when the ascending wave is in the middle of the domain. At this instant the transition to uniform flow is in progress, which makes visible that it is a smooth transition. On the east side of the wave, the water depth and velocity are approaching the expected values and the flow is successfully maintained without generating instabilities.

3.3 | Oscillations in a lake

The model is also tested in a domain with a non-trivial bathymetry. Specifically, the bottom is shaped as a parabola

$$b(x) = H_0 \left[\frac{1}{a^2} \left(x - \frac{L}{2} \right)^2 - 1 \right], \tag{60}$$

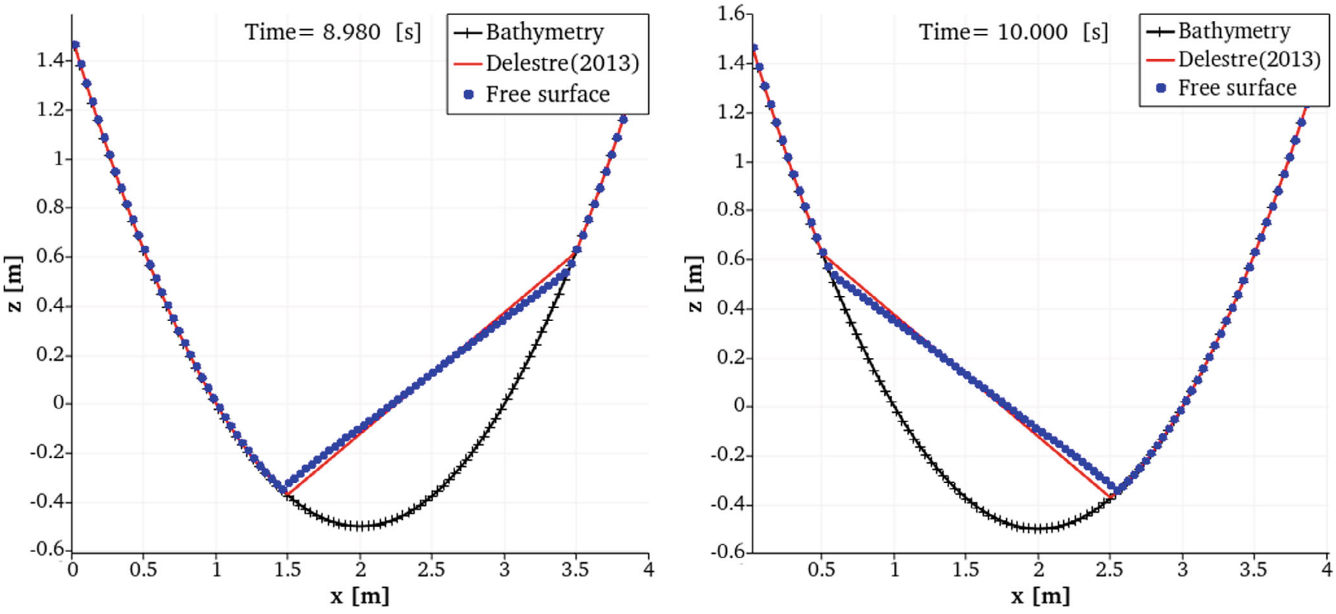

FIGURE 17 Flow of water in a parabolic lake. The cells get wet and dry cyclically. Comparison with Delestre et al. solution[64] [Colour figure can be viewed at wileyonlinelibrary.com]

where H_0 is the water depth at vertex coordinate, $L = x_E - x_W$ is the domain width, and a is a parameter for the shape of the parabola. At each time the water depth and velocity are:

$$H(t,x) = \begin{cases} -H_0\left\{\left[\frac{1}{a}\left(x-\frac{L}{2}\right)+\frac{\tilde{B}}{\sqrt{2gH_0}}\cos\left(\frac{\sqrt{2gH_0}}{a}t\right)\right]^2-1\right\} & \text{for } x_1(t) \le x \le x_2(t) \\ 0 & \text{otherwise} \end{cases}, \tag{61}$$

$$u(t,x) = \begin{cases} B\sin\frac{\sqrt{2gH_0}}{a}t & \text{for } x_1(t) \le x \le x_2(t) \\ 0 & \text{otherwise} \end{cases}, \tag{62}$$

with $\tilde{B} = \sqrt{2gH_0}/(2a)$. This particular configuration is intended to reproduce a case for which Thacker found an analytical solution for a frictionless bottom[63] in 2D, while the solution for the simplified 1D case was first provided by Delestre et al.[64] The positions of the wet/dry interfaces are denoted by $x_1(t)$ and $x_2(t)$ and read:

$$x_1(t) = -\frac{1}{2}\cos\left(\frac{\sqrt{2gH_0}}{a}t\right) - a + \frac{L}{2}, \qquad x_2(t) = -\frac{1}{2}\cos\left(\frac{\sqrt{2gH_0}}{a}t\right) + a + \frac{L}{2}. \tag{63}$$

For our simulations, we use the following setup. The water depth at the parabola vertex is set to $H_0 = 0.5$, the initial velocity is set to zero throughout the computational domain, the Strickler coefficient is chosen as $k_s = 20{,}000$ so that friction can be neglected, the maximum time step is $\Delta t_{\max} = 1 \cdot 10^{-3}$, the computational domain is $\Omega = [0, 4]$, discretized with $I_{\max} = 100$ uniform cells and the parabola shape parameter is set to $a = 1$. Two times after approximately five oscillations is shown in Figure 17. The numerical model and the analytical solution are in good agreement, but the former does not reach the same elevation at x_1 and x_2, due to numerical dissipation.

3.4 | Return to equilibrium in deep water

The aim of this test case is to verify the response of a floating body, which can for example represent a passive ship with simplified geometry, which is moved out from its equilibrium floating position at the free surface of a deep water body. The oscillation pattern of the ship should be consistent with the corresponding one in the reference solution, which is the well-known case of a damped harmonic oscillator. At the initial time, the vessel with mass m_s is out of equilibrium in still water. The forces generated by gravity and hydrostatic pressure move the vessel along the vertical direction, radiating waves. The shape of the body representing a ship is a prism with rectangular base $L_s\Delta y$. The total ship height is H_s, and the height below the center of mass G is h_s. We choose $h_s = m_s/(\rho L_s \Delta y)$, so that G will tend to the still water level (SWL). The waves would reflect at the side boundary of the water body and return to the ship, altering its oscillation pattern. To avoid this disturbance, the domain must be larger than $c_w \cdot t_{\text{end}} + L_s$, where c_w is the wave speed, t_{end} the simulation end time, and L_s the width of the ship. In this test case, we choose a large water depth H so that the effects of the added mass are reduced. It is important to stress that although we are in deep water, the model behaves equivalently to shallow water conditions. This means that the radiated waves will travel at the same speed $c_w = \sqrt{gH}$. We focus on the movement in the vertical direction only (one degree of freedom, heaving) and we neglect viscosity. The reference solution of the damped-harmonic-oscillator originates from the balance of the forces in (64):

$$(m_s + a_s)\ddot{z}_G + b_s\dot{z}_G + c_s z_G = 0, \tag{64}$$

where

$$b_s = \frac{2\rho g c_g}{\omega^2}\left(\frac{\xi_w}{z_0}\right)^2 \Delta y \qquad c_s = \rho g A_s, \tag{65}$$

$$\omega = \frac{2\pi}{T} \qquad T = 2\pi\sqrt{\frac{m_s + a_s}{\rho g A_s}}. \tag{66}$$

z_G is the elevation of the ship center of mass G, $\dot{z}_G$ is the vertical velocity of G, $\ddot{z}_G$ is its vertical acceleration. a_s is the added mass and in this case it is positive. We compute it with the equation derived by Lannes:[12]

$$a_s = \rho\, dy \int_{x_-}^{x_+} \frac{(x - \hat{x})^2}{H}\, dx, \qquad \text{with} \quad \hat{x} = \frac{1}{\int_{x_-}^{x_+} \frac{1}{H}\, dx} \int_{x_-}^{x_+} \frac{x}{H}\, dx, \tag{67}$$

where x_- and x_+ are the x coordinates of the two points P_- and P_+ where the free surface η intersects the ship, whose coordinates are (x_-, z_-) and (x_+, z_+). We also have $x_+ - x_- = L_s$, so that for this test case $a_s = \rho \Delta y L_s^3/(12H)$. c_s is the spring coefficient, derived from a combination of the Archimedes' principle and Hooke's law. The waterplane area $A_s = L_s\Delta y$ is constant. b_s is the damping coefficient for the heave motion; its expression in (65) is derived in linear wave theory considering the transfer of energy from the ship to the waves.[65] ω is the undamped natural frequency. T is the ship oscillation period, which in this test case is taken equal to the wave period. In shallow water the group velocity c_g is constant and equal to the wave speed $c_g = c_w = \sqrt{gH}$, and thus the wavelength is $L_w = T\sqrt{gH}$. z_0 is the ship oscillation amplitude and it corresponds to the initial displacement, while ξ_w is the wave amplitude and usually it is not known a priori. We observe that during a half-period the volume of water displaced by the ship V_s must be equal to the volume of the radiated wave V_w, so for this specific case we can derive an expression of the amplitude ξ_w:

$$(2z_0)\frac{L_s}{2}\Delta y = V_s = V_w = \frac{\xi_w L_w \Delta y}{\pi} \qquad \Rightarrow \qquad \xi_w = \frac{\pi z_0 L_s}{L_w}. \tag{68}$$

We substitute c_g, ω and ξ_w in (65) and obtain the damping coefficient b_s expressed in terms of known quantities:

$$b_s = \frac{\rho g L_s^2 \Delta y}{2\sqrt{gH}}. \tag{69}$$

We define $\sigma = \dfrac{b_s}{2(m_s + a_s)}$ and we rewrite Equation (64) in a canonical form:

$$\ddot{z}_G + 2\sigma\dot{z}_G + \omega^2 z_G = 0. \tag{70}$$

The solution of (70) is

$$z_G(t) = z_0 e^{-\sigma t}\left[\cos(\omega_z t) + \frac{\sigma}{\omega_z}\sin(\omega_z t)\right], \tag{71}$$

with $w_z = \sqrt{w^2 - \sigma^2}$. The velocity is then:

$$\dot{z}_G(t) = -z_0 e^{-\sigma t}\left(\omega_z + \frac{\sigma^2}{\omega_z}\right)\sin(\omega_z t). \tag{72}$$

The simulation parameters are given in Table 1. The initial configuration can be seen in Figure 18 and the results are in Figures 19 and 20. The oscillation pattern is in good agreement with the reference solution.

We want to provide an interpretation of how the fluid-structure coupling dampens the oscillation implicitly. The dampening is the result of a restoring force that is consistently smaller than what would be required to keep the amplitude of oscillation constant. Such force is a function of the equilibrium position z_{eq} of the ship and the instantaneous value of η at the waterline, the point of intersection of the ship and the waves. For the damped-harmonic-oscillator reference

TABLE 1 Data for the return to equilibrium in deep water test case

Symbol	Definition	Value	Unit of measurement
η_0	Initial free surface elevation (SWL)	0	m
u	Initial horizontal velocity	0	m/s
b	Bottom	−1000	m
k_s	Strickler coefficient	100	$m^{\frac{1}{3}}/s$
s	Subcells in each cell	4	-
θ	Implicitness factor	1	-
Δt	Time step size (constant)	$1 \cdot 10^{-3}$	s
Δx	Grid size along x	2.5	m
z_0	Initial displacement of the ship	−2	m
m_s	Ship mass	100,000	kg
L_s	Ship length	20	m
Δy	Ship width	1	m
H_s	Total ship height	10	m

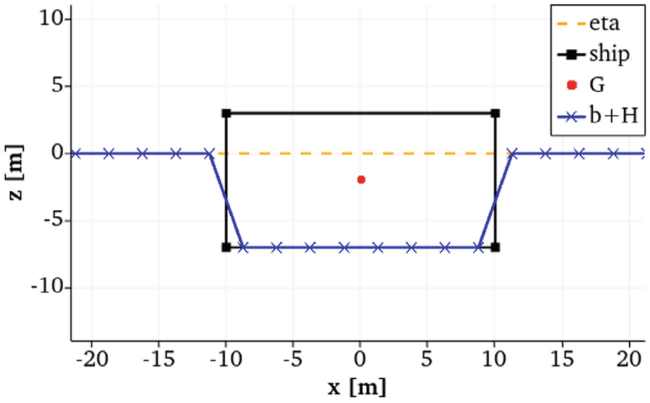

FIGURE 18 Initial configuration of the return to equilibrium test case. The figure shows only the area near the ship, even though the domain is larger and higher. [Colour figure can be viewed at wileyonlinelibrary.com]

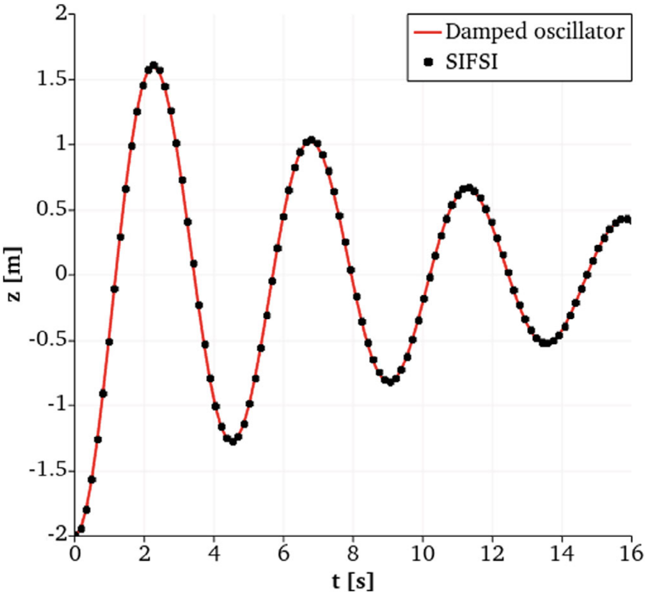

FIGURE 19 Time evolution of the ship elevation in the test case of return to equilibrium in deep water. The elevation of the center of mass z_G is compared to the expected value from the damped-oscillator solution. [Colour figure can be viewed at wileyonlinelibrary.com]

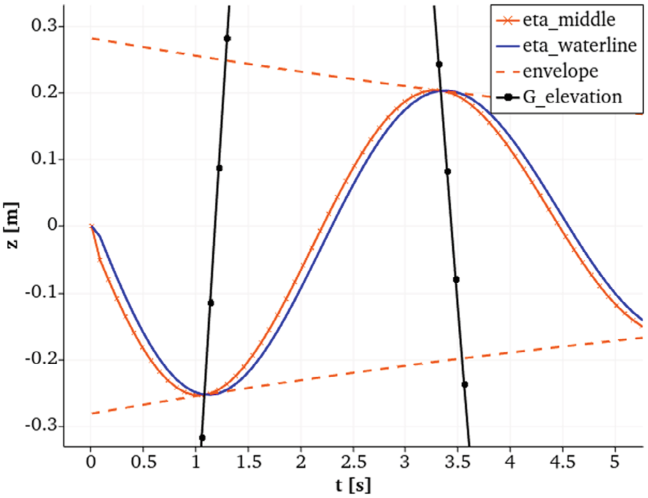

FIGURE 20 Time evolution of η in the middle of the ship and at the waterline, in the test case of return to equilibrium in deep water. The z_G curve is shown only in the range of interest of the vertical axis, where we want to highlight the points of intersection with the η curves; the full curve is in Figure 19. The dashed lines are the envelope of the wave amplitude. [Colour figure can be viewed at wileyonlinelibrary.com]

solution, z_{eq} is assumed at the SWL, and thus the instant force is simply proportional to $z_{eq} - z_G(t)$. What makes the oscillator "damped" is the addition to the ODE of the radiation resistance force $b_s \dot{z}_G$, and the additional inertia of the motion in water is introduced by means of the added mass a_s. On the contrary, with a fluid-structure coupling the radiated waves move the position of the waterline, meaning that z_{eq} is time dependent and specifically it oscillates together with η, so the net vertical force is given by (36). When the ship is accelerating upwards, η at the waterline decreases and the pressure distribution is concave up. The vertical force is lower than it would be if the equilibrium position was fixed at the SWL, so the oscillation is damped. Of course, when the ship is accelerating downwards the opposite is true: η at the waterline increases and its concavity is down, but the effect is again a dampening of the oscillation. In this specific test case there is vertical symmetry, so when the acceleration of the ship is zero the pressure η inside the ship is almost horizontal everywhere. It follows that in this precise moment the outgoing waves are at their minimum or maximum elevation, called trough and crest. For our specific choice of h_s, when the acceleration is zero it also means that $z_G = \eta$.

We can relate the interpretation above to the results in Figure 20. We can see that while $z_G < \eta$, which is when the ship is accelerating upwards, η in the middle of the ship is lower than the η at the waterline, which indicates that η is concave up. When $z_G \approx \eta$, the distribution of η is, in first approximation, horizontal. When $z_G > \eta$, η is concave down. We can also see that for the first half of the oscillation period, $\eta <$ SWL, which means that the upward force on the hull is always smaller than it would be without the fluid-structure interaction, and this causes the dampening. In the second half oscillation period, $\eta >$ SWL, the upward force on the hull is always bigger that it would be without the FSI, so the downward descent is slowed down.

From the time evolution of η in Figure 20 we can also get information on the generation of radiated waves, because η has the meaning of piezometric head in the ship region, and of free-surface outside the ship region. The waves in this test case start from the symmetry point, the center of the ship, and radiate outwards. We know the value of the wave amplitude from Equation (68), and we can expect that it will be damped of a factor $\mathrm{e}^{-\sigma t}$, as the ship oscillation amplitude. The envelope of η at the ship center is computed from Equation (73):

$$\Xi_w(t) = \xi_w \mathrm{e}^{-\sigma t}. \tag{73}$$

The value predicted by Equation (73) corresponds to the numerical wave trough and crest. We also observe that the curves of η in the middle of the ship and η at the waterline are almost overlapping; this happens because the wave speed c_w is high, so the time delay $(L_s/2)/c_w$ between the two is small.

3.5 | Return to equilibrium in shallow water

In this test case, we want to look at the effects of a smaller water depth H on the oscillation pattern. The reference solution is formally equal to the solution in Section 3.4. With a smaller water depth, the solid boundary is closer to the ship, so we expect an increased contribution of the added mass.[66] The effect of a_s (it's value is always positive), looking at the definitions of T and σ in Section 3.4, is to increase the period of oscillation and reduce the damping coefficient. However, this does not necessarily mean that the overall damping is smaller, because from Equation (69) we see that b_s increases as H decreases. In fact, generally the damping is stronger in shallow water.[67] The parameters for this test case are the same as in the previous one, Table 1, with the only exception of setting the bottom at $b = -20$ m. The time evolution of z_G is shown in Figure 21. In shallow water the oscillation is more damped than it is in deep water, and we have a good agreement with the analytical solution again. Figure 22 displays the time evolution of η in the ship region. Most of the considerations done for the deep water test case in Section 3.4 are still true, but there are some important differences. First, the amplitude is bigger, which is the reason for the increased dampening. Second, the wave speed is lower, which means that the peaks of the curves of η are shifted in time. The consequence of this time delay is that the concavity of η is much more pronounced. Also, in this time period the ship is heaving and its motion seems to deform the outgoing wave, reducing its peaks; now, the envelope of Equation (73) predicts well only η in the middle of the ship. An interesting observation can be done if we separate the dampening into two components, one being the variation of η at the waterline and the second one being the concavity of η. The former is equivalent to assuming that η is a straight line connecting the intersection points P_- and P_+, the latter is the deviation from this straight line. In this test case, thanks to the symmetry of the problem, we can separate the two components also in the numerical simulation: when computing the vertical force, we assume η constant inside the ship and equal to the value at the waterline. If we do that, we are removing the component due to the concavity of η. What we observe from the results in Figure 23 is that this numerical solution matches the reference solution with $a_s = 0$, meaning that the period of oscillation is smaller and the oscillation is more damped. This experiment would suggest that the "linear" component of η has the equivalent effect of the damping coefficient b_s in the ODE, while the curvature of η has the equivalent effect of the added mass a_s. We can do one more observation on the concavity of η, which is related to its steepness. From the momentum Equation (13) we derive the expression (74) for the gradient of pressure.

$$\frac{\Delta\eta}{\Delta x} = \frac{q^* - q^{n+1}}{gH\Delta t}. \tag{74}$$

The gradient depends on the space and time flux derivatives and it is inversely proportional to the water depth. It follows that in shallow water the curvature of η is more pronounced, which is what we observed from the numerical simulations.

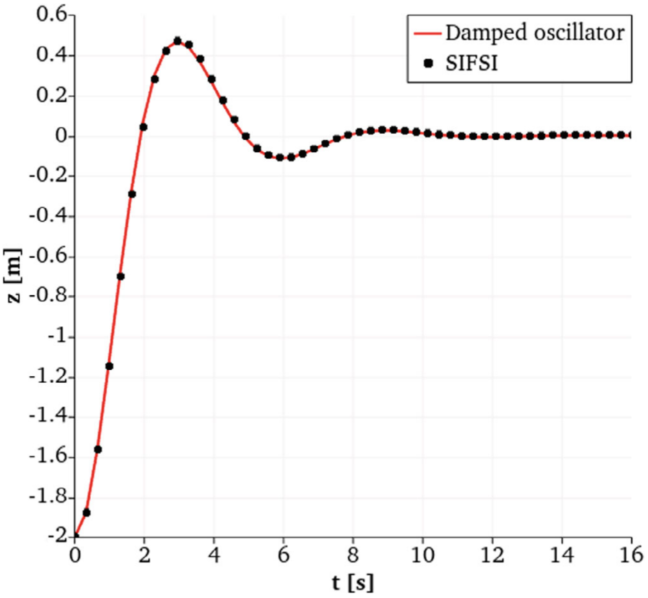

FIGURE 21 Time evolution of the ship elevation in the test case of return to equilibrium in shallow water. The elevation of the center of mass z_G is compared to the expected value from the damped-oscillator solution. [Colour figure can be viewed at wileyonlinelibrary.com]

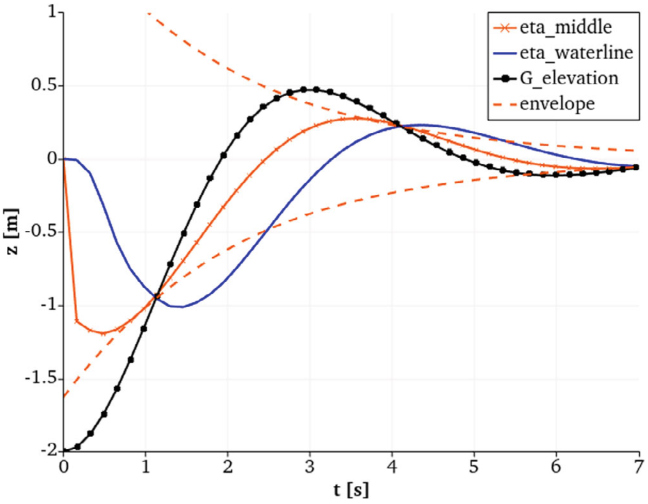

FIGURE 22 Time evolution of η in the middle of the ship and at the waterline, in the test case of return to equilibrium in shallow water. The dashed lines are the envelope of the wave amplitude. [Colour figure can be viewed at wileyonlinelibrary.com]

3.6 | Heaving due to incoming waves

In this test case, we analyze the response of a trapezoidal ship to the influence of regular incoming waves produced by a wavemaker. The sinusoidal waves are generated at the west boundary of the water body containing the ship, forming a numerical wave tank. At the initial time, the ship floats in its hydrostatic equilibrium position close to the west boundary of the tank. The ship has a flat bottom of length L_{bottom} and oblique sides inclined of an angle α_s from the vertical. Due to the shape of the ship, the immersed volume is not directly proportional to the vertical displacement. We choose the position of the east boundary to make sure the reflected waves do not reach back the ship during the simulation time. The water depth is the same used in the return-to-equilibrium in shallow-water test case, in Section 3.5. Again, we concentrate on the ship movement with one degree of freedom, namely on the vertical heaving. The physical reference case is a forced and damped oscillator, described by the second order ODE (75), which is a generalization of Equation (64). ODE (75) allows

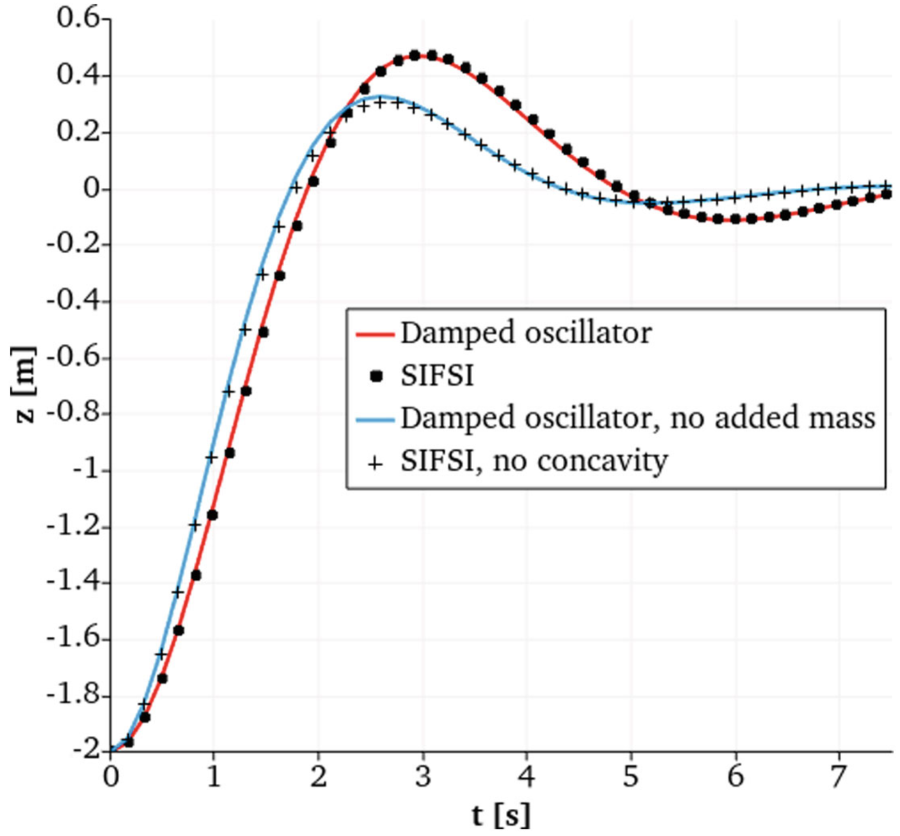

FIGURE 23 Effect of the concavity of η on the ship motion. If only the linear component of η is used to compute the vertical force, the numerical results agree with the reference solution with $a_s = 0$. [Colour figure can be viewed at wileyonlinelibrary.com]

for both rectangular and trapezoidal shapes of the ship, an arbitrary initial still water level, an arbitrary relative position of the center of mass and a delayed external forcing by regular waves. We apply the so-called small-body approximation,[68] which states that the length of the floating body is much smaller than the wave length ($L_{wl} \ll T_w \cdot c_w$). The solution is found numerically using a Runge–Kutta fourth-order scheme.

$$\begin{cases} (m_s + a_s)\ddot{z}_G + b_s\dot{z}_G + c_s z_G - \epsilon z_G^2 = c_s\left(\eta_0 + \frac{H_w}{2}\sin(\omega_w(t-t_0)) + h_s\right) - \epsilon\left(\eta_0 + \frac{H_w}{2}\sin(\omega_w(t-t_0)) + h_s\right)^2 - m_s g \\ \dot{z}_G(t = t_0) = 0 \\ z_G(t = t_0) = \eta_0 - D_{eq} + h_s \end{cases}, \tag{75}$$

where m_s is the ship mass, η_0 is the free-surface elevation at the start of simulation, H_w is the incoming wave height, $\omega_w = 2\pi/T_w$ is the wave frequency, h_s is the vertical distance between the center of mass G and the bottom of the ship. The added mass a_s and the damping coefficient b_s are defined as in Section 3.4. For b_s, we use the water depth defined by the current free-surface elevation near the ship, and as length the length at the water level $L_{wl} = L_{\text{bottom}} + 2\tan(\alpha_s)D_{eq}$, where the draft at equilibrium D_{eq} is the solution of:

$$\tan(\alpha_s)D_{eq}^2 + L_{\text{bottom}}D_{eq} - \frac{m_s}{\rho\Delta y} = 0. \tag{76}$$

The terms c_s and ϵ are:

$$c_s = \rho g\Delta y\left[L_{\text{bottom}} + 2\tan(\alpha_s)\left(\eta_0 + \frac{H_w}{2}\sin(\omega_w(t-t_0)) + h_s\right)\right] \qquad \epsilon = \rho g\Delta y\tan(\alpha_s). \tag{77}$$

The reference solution is delayed in time because the incoming waves generated at the west boundary reach the ship side at

$$t_0 = \frac{1}{c_w}\left[x_G - \left(\frac{L_{\text{bottom}}}{2} + \tan(\alpha_s)D_{eq}\right) - x_W\right].$$

When the waves pass by the ship position, the instantaneous equilibrium position changes in time and a restoring force acts on the hull, but the ship stays outside the position of equilibrium. As a result, the wave elevation and the ship response are shifted in time of t_{ws}. This delay in time can be obtained, with accuracy sufficient for our purposes, from the analytical solution of an equivalent problem with a rectangular ship:

$$t_{ws} = \frac{1}{\omega_w}\arctan\left(\frac{b_s\omega_w}{(m_s + a_s)\omega_w^2 - 0.5\rho g\Delta y(L_{wl} + L_{\text{bottom}})}\right). \tag{78}$$

It is possible to show, by substituting the value of b_s in (78) and assuming ω_w and $\tan(\alpha_s)D_{eq}$ are small, that this time delay is approximately the time necessary for the wave to travel half of the ship length at the waterline:

$$t_{ws} \approx -\frac{1}{c_w}\left(\frac{L_{\text{bottom}}}{2} + \tan(\alpha_s)D_{eq}\right). \tag{79}$$

To check the presence of the time delay t_{ws}, we will plot the motion of a ship always in equilibrium with the current wave elevation at the west ship side, which is equivalent to a simple harmonic oscillator with a heave amplitude and period equal to the ones of the incoming wave:

TABLE 2 Data for the heaving due to incoming waves test case

Symbol	Definition	Value	Unit of measurement
η_0	Initial free surface elevation (SWL)	0	m
u	Initial horizontal velocity	0	m/s
b	Bottom	−20	m
k_s	Strickler coefficient	100	$m^{\frac{1}{3}}/s$
s	Subcells in each cell	4	-
θ	Implicitness factor	1	-
Δt	Time step size (constant)	0.01	s
Δx	Grid size along x	1	m
z_0	Initial vertical displacement of the ship	0	m
m_s	Ship mass	100,000	kg
L_{bottom}	Ship length at bottom	20	m
L_{top}	Ship length at top	40	m
Δy	Ship width	1	m
H_s	Total ship height	10	m
H_w	Wave height	1	m
T_w	Wave period	24	s

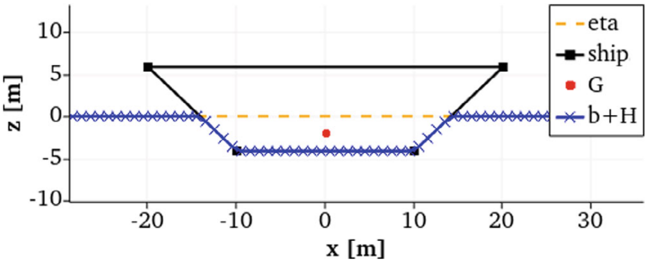

FIGURE 24 Initial configuration of the heaving due to incoming waves test case. The figure shows only the area near the ship, even though the domain is larger and higher. [Colour figure can be viewed at wileyonlinelibrary.com]

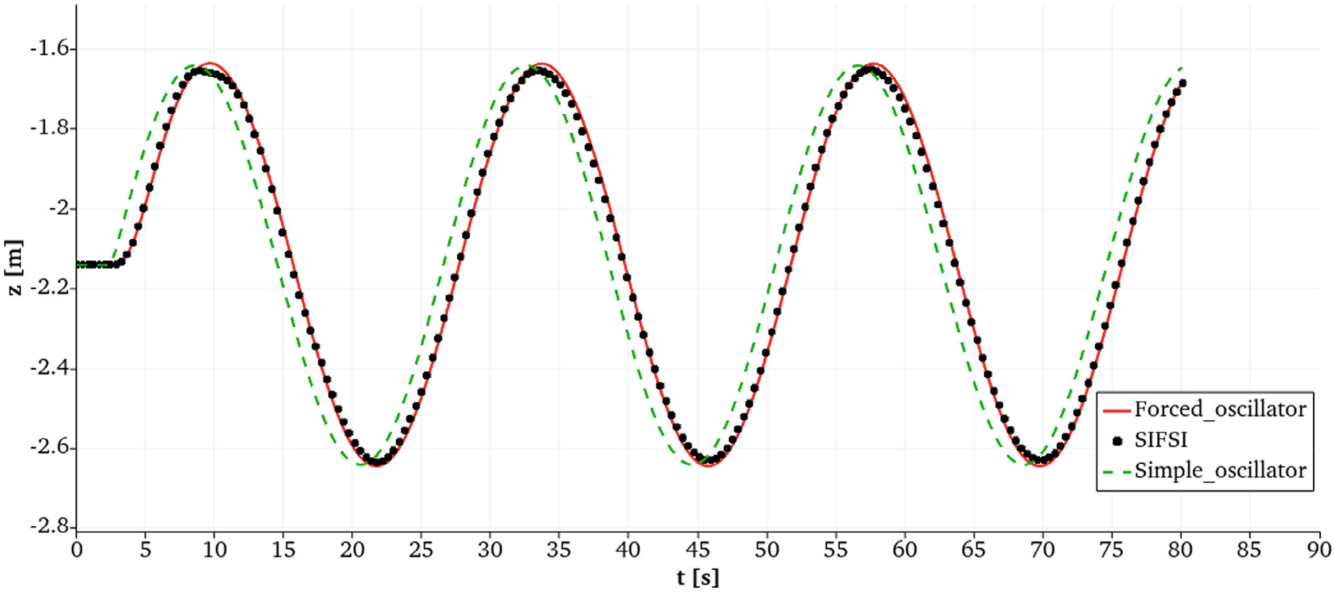

FIGURE 25 Time evolution of the ship elevation in a test case with incoming waves in shallow water. The elevation of the center of mass z_G is compared to the expected value from the forced and damped oscillator solution. In addition, the simple oscillator solution shows the time delay between the wave elevation and the ship response. [Colour figure can be viewed at wileyonlinelibrary.com]

$$z_G(t) = z_G(0) + \frac{H_w}{2}\sin(\omega_w(t - t_0)) \qquad \text{for } \ t \geq t_0. \tag{80}$$

The data for the simulation are summarized in Table 2, while a view of the initial conditions is shown in Figure 24. The numerical results are compared to the reference solutions in Figure 25. The numerical and reference solution agree fairly well with each other. This is true starting from the first oscillation, when the ship has to adjust to a sinusoidal motion from the initial equilibrium conditions. We observe that there is the time delay between the wave passage and the ship response, which for this test case was predicted as $t_{ws} = 1.33$ s. We notice that the oscillation pattern has the same amplitude of the incoming waves; the natural oscillation of the ship, whose time period is computed from Equation (66) and is equal to $T_s = 5.7$ s, is damped. There are small errors at the highest and lowest elevation points. Namely, the oscillation amplitude is slightly smaller compared to the reference solution. The probable cause is that the problem solved with the new model is more general than the reference problem. Some additional physical and numerical processes deform the waves in the simulation: first, the waves that hit the ship are partially reflected back, so less pressure acts on the hull; second, even though the small-body assumption holds, in the ship region we never have uniform values of the piezometric head, which means its average value is never as high as the value in the reference problem; third, while the waves are traveling from the west boundary to the ship, they are affected by numerical dissipation and their peaks are damped. These three effects, which would slightly reduce the oscillation amplitude, are not included in the reference ODE (75).

4 | CONCLUSIONS AND OUTLOOK

In this article a novel staggered semi-implicit finite volume scheme for the numerical solution of fluid-structure-interaction problems was presented. In particular, the interaction of hydrostatic geophysical free surface flows with floating ships was studied. The ship was considered as a rigid body with 6 degrees of freedom and its dynamics was described at the aid of a first order system of ordinary differential equations. The PDE and ODE systems communicate with each other through the nonlinear volume function in the discrete hydrodynamics equations and the pressure field which provides the forces for the rigid body dynamics. The approach presented in this article is based on the hydrostatic pressure assumption and is therefore computationally very efficient compared to a fully nonhydrostatic 3D CFD simulation of the flow around floating ships. Wetting and drying process is part of the algorithm, making it is possible to study bodies of water ranging from rivers and lakes to the open sea. Computational accuracy has been enhanced using subgrid techniques which act on the bottom bathymetry and on the geometry of the ship; the result is a balance between accuracy and speed, and flexibility according to the user needs. An important part of the model development was the verification against theoretical solutions known for simplified cases. When there are no floating objects, the model give the results that we would expect from a usual shallow water model. When we include floating objects, we showed, for the vertical degree of freedom, that their response is consistent with the solution of the reference problems. Additionally, the damping and the added mass forces are naturally included, without the need to model them. The radiated waves generated by the fluid-structure interaction, tested during heaving, are coherent with the analytical values. Mass and linear momentum conservation is ensured globally and locally at all-time steps.

In the following, we provide a brief outlook to potential future work and improvements. Starting from the model developed in this article, it is possible to progress in many ways:

- Add more verification tests of the degress of freedom of the floating object.
- Obtain a more realistic ship dynamics model, considering propulsion, steering and drag forces.
- Investigate the reproductions of ship-bank effects, ship induced waves interacting with banks, the squat of a ship in motion, ship-ship interactions[47] and interactions of the ship with a lock.
- Validate the model in the case of river flows, using simulations with input data (bathymetry, friction coefficients, shape and mass distribution of the ship, boundary conditions) from real test cases. The ship geometry could be read, for example, in the form of a surface triangulation (STL file) and the river bathymetry defined from available Digital Elevation Models (DEM) at the subgrid level of varying accuracy.
- Extend the range of applications of the model, updating the hydrostatic pressure with a fully nonhydrostatic pressure correction approach according to the seminal work of Casulli,[69] which is in principle similar to the SIMPLE method of Patankar and Spalding,[70] but with a particularly sophisticated initial guess for the pressure based on the efficient solution of the underlying hydrostatic problem. Alternatively, it is possible to introduce dispersive effects applying a Boussinesq-type formulation of the system. If both methods were implemented, it would be very interesting to compare them in terms of computational costs and accuracy, and determine the operating conditions that produce similar results.
- Increase the space-time order of accuracy of the method, for example using IMEX schemes[71] as well as higher order discontinuous Galerkin finite element methods.[36]
- Improve efficiency and code speed using high performance computing techniques. The parallelization of the code with the integration of the message passing interface (MPI) allows to run the simulations on massively parallel distributed memory supercomputers.

ACKNOWLEDGMENT

This project is part of a collaboration between the University of Trento and *Bundesanstalt für Wasserbau* (BAW, German Federal Waterways Engineering and Research Institute). The authors want to thank Jacek A. Jankowski and Michael Schröder (BAW Karlsruhe) for their helpful suggestions and the vivid interest in each phase of development of the model. In addition, we want to thank Arturo De Marinis for his constant presence and morale support. This research was funded by the Italian Ministry of Education, University and Research (MIUR) in the frame of the Departments of Excellence Initiative 2018–2022 attributed to DICAM of the University of Trento (grant L. 232/2016) and in the frame of the PRIN 2017 project *Innovative numerical methods for evolutionary partial differential equations and applications*. M.D. is member of the INdAM GNCS group. The authors are very grateful to the two anonymous referees for their constructive comments and remarks, which helped to improve the quality and readability of this article. Open Access Funding provided by Universita degli Studi di Trento within the CRUI-CARE Agreement.

DATA AVAILABILITY STATEMENT

The data that support the findings of this study are available from the corresponding author upon reasonable request.

ORCID

Cristian Brutto https://orcid.org/0000-0002-0492-875X
Michael Dumbser https://orcid.org/0000-0002-8201-8372

REFERENCES

1. Bradford SF. Nonhydrostatic model for free surface flow interaction with structures. *Int J Numer Methods Fluids*. 2021;93(8):2508-2530. doi:10.1002/fld.4985
2. Shao Y, Zheng Z, Liang H, Chen J. A consistent second-order hydrodynamic model in the time domain for floating structures with large horizontal motions. *Comput Aided Civ Inf Eng*. 2022;37(7):894-914. doi:10.1111/mice.12782
3. Tong C, Shao Y, Bingham H. Modeling fully nonlinear wave-structure interaction by an adaptive harmonic polynomial cell method with immersed boundaries. Proceedings of the 36th International Workshop on Water Waves and Floating Bodies. 2021.
4. Ferrari D, Dumbser M. A mass and momentum-conservative semi-implicit finite volume scheme for complex non-hydrostatic free surface flows. *Int J Numer Methods Fluids*. 2021;93(9):2946-2967. doi:10.1002/fld.5017
5. Gaburro E, Castro M, Dumbser M. A well balanced diffuse interface method for complex nonhydrostatic free surface flows. *Comput Fluids*. 2018;175:180-198.
6. Kemm F, Gaburro E, Thein F, Dumbser M. A simple diffuse interface approach for compressible flows around moving solids of arbitrary shape based on a reduced Baer-Nunziato model. *Comput Fluids*. 2020;204:104536.
7. Preissmann A, Cunge JA. Calcul des intumescences Sur machinas electroniques. *Proceedings of 9th Congress of International Association for Hydraulic Research (IAHR).* 1961:656-664.
8. Cunge JA, Wegner M. Numerical integration of Barré de saint-Venant's flow equations by means of an implicite scheme of finite differences. Applicants in the case of alternately free and pressurised flow in a tunnel. *La Houille Blanche*. 1964;50(1):33-39. doi:10.1051/lhb/1964002
9. Vasconcelos JG, Wright SJ, Roe PL. Improved simulation of flow regime transition in sewers: two-component pressure approach. *J Hydraul Eng*. 2006;132(6):553-562. doi:10.1061/(ASCE)0733-9429(2006)132:6(553)
10. Bousso S, Daynou M, Fuamba M. Numerical Modeling of mixed flows in storm water systems: critical review of literature. *J Hydraul Eng*. 2013;139(4):385-396. doi:10.1061/(ASCE)HY.1943-7900.0000680
11. Bosi U, Engsig-Karup AP, Eskilsson C, Ricchiuto M. A spectral/hp element depth-integrated model for nonlinear wave–body interaction. *Comput Methods Appl Mech Eng*. 2019;348:222-249. doi:10.1016/j.cma.2019.01.020
12. Lannes D. On the dynamics of floating structures. *Annal PDE*. 2017;3(1):11. doi:10.1007/s40818-017-0029-5
13. Godlewski E, Parisot M, Sainte-Marie J, Wahl F. Congested shallow water model: roof modeling in free surface flow. *Esaim: M2AN*. 2018;52(5):1679-1707. 10.1051/m2an/2018032
14. Godlewski E, Parisot M, Sainte-Marie J, Wahl F. Congested shallow water model: on floating body. *The SMAI J Comput Math*. 2020;6:227-251. doi:10.5802/smai-jcm.67
15. Bocchi E, He J, Vergara HG. Modelling and simulation of a wave energy converter. *ESAIM Proc Surv*. 2021;70:68-83. doi:10.1051/proc/202107005
16. Soomere T. Nonlinear components of ship wake waves. *Appl Mech Rev*. 2007;60(3):120-138. doi:10.1115/1.2730847
17. Casulli V, Stelling GS. Numerical simulation of 3D quasi-hydrostatic, free-surface flows. *J Hydraul Eng*. 1998;124(7):678-686. doi:10.1061/(ASCE)0733-9429(1998)124:7(678)
18. Stansby PK, Zhou JG. Shallow-water flow solver with non-hydrostatic pressure: 2D vertical plane problems. *Int J Numer Methods Fluids*. 1998;28(3):541-563. doi:10.1002/(SICI)1097-0363(19980915)28:3<541::AID-FLD738>3.0.CO;2-0
19. Madsen P, Murray R, Sørensen O. A new form of the Boussinesq equations with improved linear dispersion characteristics. *Coast Eng*. 1991;15:371-388.
20. Madsen PA, Sørensen OR. A new form of the Boussinesq equations with improved linear dispersion characteristics. Part 2. A slowly-varying bathymetry. *Coast Eng*. 1992;18(3):183-204. doi:10.1016/0378-3839(92)90019-Q
21. Madsen P, Bingham H, Schäffer H. Boussinesq-type formulations for fully nonlinear and extremely dispersive water waves: derivation and analysis. *Proc R Soc London Ser A*. 2003;459:1075-1104.
22. Rijnsdorp DP, Zijlema M. Simulating waves and their interactions with a restrained ship using a non-hydrostatic wave-flow model. *Coast Eng*. 2016;114:119-136. doi:10.1016/j.coastaleng.2016.04.018
23. Zijlema M, Stelling GS. Further experiences with computing non-hydrostatic free-surface flows involving water waves. *Int J Numer Methods Fluids*. 2005;48(2):169-197. doi:10.1002/fld.821

24. Bingham H. A hybrid Boussinesq-panel method for predicting the motion of a moored ship. *Coast Eng*. 2000;40(1):21-38. doi:10.1016/S0378-3839(00)00002-8
25. Karambas T, Loukogeorgaki E. A Boussinesq-type model for nonlinear wave-heaving cylinder interaction. *Energies*. 2022;15(2):469. doi:10.3390/en15020469
26. Beck G, Lannes D. Freely floating objects on a fluid governed by the Boussinesq equations. *Ann Inst Henri Poincare C Anal Non Lineaire*. 2022;39(3):575-646. doi:10.4171/aihpc/15
27. Engsig-Karup A, Hesthaven J, Bingham H, Warburton T. DG-FEM solution for nonlinear wave-structure interaction using Boussinesq-type equations. *Coast Eng*. 2008;55:197-208.
28. Favrie N, Gavrilyuk S. A rapid numerical method for solving serre-green-Naghdi equations describing long free surface gravity waves. *Nonlinearity*. 2017;30:2718-2736.
29. Escalante C, Dumbser M, Castro M. An efficient hyperbolic relaxation system for dispersive non-hydrostatic water waves and its solution with high order discontinuous Galerkin schemes. *J Comput Phys*. 2019;394:385-416.
30. Escalante C, Morales T. A general non–hydrostatic hyperbolic formulation for Boussinesq dispersive shallow flows and its numerical approximation. *J Sci Comput*. 2020;83:62.
31. Bassi C, Bonaventura L, Busto S, Dumbser M. A hyperbolic reformulation of the serre-green-Naghdi model for general bottom topographies. *Comput Fluids*. 2020;212:104716.
32. Busto S, Dumbser M, Escalante C, Gavrilyuk S, Favrie N. On high order ADER discontinuous Galerkin schemes for first order hyperbolic reformulations of nonlinear dispersive systems. *J Sci Comput*. 2021;87:48.
33. Casulli V, Stelling GS. A semi-implicit numerical model for urban drainage systems. *Int J Numer Methods Fluids*. 2013;73(6):600-614. doi:10.1002/fld.3817
34. Casulli V, Walters RA. An unstructured grid, three–dimensional model based on the shallow water equations. *Int J Numer Methods Fluids*. 2000;32:331-348.
35. Casulli V, Stelling GS. Semi-implicit subgrid modelling of three-dimensional free-surface flows. *Int J Numer Methods Fluids*. 2011;67(4):441-449. doi:10.1002/fld.2361
36. Tavelli M, Dumbser M. A high order semi-implicit discontinuous Galerkin method for the two dimensional shallow water equations on staggered unstructured meshes. *Appl Math Comput*. 2014;234:623-644.
37. Busto S, Ferrín JL, Toro EF, Vázquez-Cendón ME. A projection hybrid high order finite volume/finite element method for incompressible turbulent flows. *J Comput Phys*. 2018;353:169-192.
38. Ioriatti M, Dumbser M. A posteriori sub-cell finite volume limiting of staggered semi-implicit discontinuous Galerkin schemes for the shallow water equations. *Appl Numer Math*. 2019;135:443-480.
39. Busto S, Dumbser M. A staggered semi-implicit hybrid finite volume/finite element scheme for the shallow water equations at all Froude numbers. *Appl Numer Math*. 2022;175:108-132.
40. Río-Martín L, Busto S, Dumbser M. A massively parallel hybrid finite volume/finite element scheme for computational fluid dynamics. *Mathematics*. 2021;9:2316.
41. Brugnano L, Casulli V. Iterative solution of piecewise linear systems. *SIAM J Sci Comput*. 2007;30:463-472.
42. Brugnano L, Casulli V. Iterative solution of piecewise linear systems and applications to flows in porous media. *SIAM J Sci Comput*. 2009;31:1858-1873.
43. Casulli V, Zanolli P. A nested Newton-type algorithm for finite volume methods solving Richards' equation in mixed form. *SIAM J Sci Comput*. 2010;32(4):2255-2273. doi:10.1137/100786320
44. Casulli V, Zanolli P. Iterative solutions of mildly nonlinear systems. *J Comput Appl Math*. 2012;236(16):3937-3947. doi:10.1016/j.cam.2012.02.042
45. Casulli V. A high-resolution wetting and drying algorithm for free-surface hydrodynamics. *Int J Numer Methods Fluids*. 2009;60(4):391-408. doi:10.1002/fld.1896
46. Chen XN, Sharma SD. A slender ship moving at a near-critical speed in a shallow channel. *J Fluid Mech*. 1995;291:263-285. doi:10.1017/S0022112095002692
47. Vantorre M, Eloot K, Delefortrie G, Lataire E, Candries M, Verwilligen J. Encyclopedia of maritime and offshore engineering. *Maneuvering in Shallow and Confined Water*. John Wiley & Sons, Ltd; 2017:1-17. doi:10.1002/9781118476406.emoe006
48. Giorgi G, Penalba M, Ringwood J. Nonlinear hydrodynamic models for heaving buoy wave energy converters. *Proceedings of the Asian Wave and Tidal Energy Conference*. Research Publishing; 2016:1-10.
49. Te Chow V. *Open-Channel Hydraulics*. Civil Engineering Series. McGraw-Hill; 1959.
50. Stelling GS, Duinmeijer SPA. A staggered conservative scheme for every Froude number in rapidly varied shallow water flows. *Int J Numer Methods Fluids*. 2003;43(12):1329-1354. doi:10.1002/fld.537
51. Rusanov V. The calculation of the interaction of non-stationary shock waves and obstacles. *USSR Comput Math Math Phys*. 1962;1(2):304-320. doi:10.1016/0041-5553(62)90062-9
52. Courant R, Friedrichs K, Lewy H. Über die partiellen Differenzengleichungen der mathematischen Physik. *Math Ann*. 1928;100:32-74. doi:10.1007/BF01448839
53. Casulli V, Dumbser M, Toro E. Semi–implicit numerical modelling of axially symmetric flows in compliant arterial systems. *Int J Numer Methods Biomed Eng*. 2012;28:257-272.
54. Bermúdez A, Vázquez-Cendón ME. Upwind methods for hyperbolic conservation Laws with source terms. *Comput Fluids*. 1994;23(8):1049-1071.

55. Castro M, Gallardo J, Parés C. High order finite volume schemes based on reconstruction of states for solving hyperbolic systems with nonconservative products. Applications to shallow-water systems. *Math Comput*. 2006;75:1103-1134. doi:10.1090/S0025-5718-06-01851-5
56. Stoker J. *Water Waves: The Mathematical Theory with Applications*. Pure and applied mathematics. Interscience Publishers; 1957.
57. Toro E. *Shock-Capturing Methods for Free-Surface Shallow Flows*. John Wiley & Sons; 2001.
58. Ritter A. Die fortpflanzung der wasserwellen. *Z Ver Dtsch Ing*. 1892;36(33):947-954.
59. Castro-Orgaz O, Chanson H. Ritter's dry-bed dam-break flows: positive and negative wave dynamics. *Environ Fluid Mech*. 2017;17:665-694. doi:10.1007/s10652-017-9512-5
60. Kramer SC, Stelling GS. A conservative unstructured scheme for rapidly varied flows. *Int J Numer Methods Fluids*. 2008;58:183-212.
61. Gauckler P. Etudes Théoriques et Pratiques Sur l'Ecoulement et le Mouvement des Eaux. *Compt R Acad Sci*. 1867;64:818-822.
62. Manning R. On the flow of water in open channels and pipes. *Trans Inst Civil Eng Irel*. 1891;20:161-207.
63. Thacker WC. Some exact solutions to the nonlinear shallow-water wave equations. *J Fluid Mech*. 1981;107:499-508. doi:10.1017/S0022112081001882
64. Delestre O, Lucas C, Ksinant PA, et al. SWASHES: a compilation of shallow water analytic solutions for hydraulic and environmental studies. *Int J Numer Methods Fluids*. 2013;72(3):269-300. doi:10.1002/fld.3741
65. Journée J, Massie W. *Offshore Hydromechanics*. Delft University of Technology; 2001.
66. Brennen CA. *Review of Added Mass and Fluid Inertial Forces. Technical Report*. Department of the Navy; 1982.
67. Kim CH. *The Influence of Water Depth on the Heaving and Pitching Motions of a Ship Moving in Longitudinal Regular Head Waves*. Technical Report 44. Chalmers University of Technology, Department of Naval Architecture and Marine Engineering, Division of Ship Hydromechanics; 1968.
68. Pecher A, Kofoed J. *Handbook of Ocean Wave Energy*. Springer; 2017.
69. Casulli V. A semi-implicit finite difference method for non-hydrostatic, free-surface flows. *Int J Numer Methods Fluids*. 1999;30(4):425-440. doi:10.1002/(SICI)1097-0363(19990630)30:4%3C425::AID-FLD847%3E3.0.CO;2-D
70. Patankar S, Spalding D. A calculation procedure for heat, mass and momentum transfer in three-dimensional parabolic flows. *Int J Heat Mass Transf*. 1972;15(10):1787-1806. doi:10.1016/0017-9310(72)90054-3
71. Boscheri W, Pareschi L. High order pressure-based semi-implicit IMEX schemes for the 3D Navier-stokes equations at all Mach numbers. *J Comput Phys*. 2021;434:110206. doi:10.1016/j.jcp.2021.110206

How to cite this article: Brutto C, Dumbser M. A semi-implicit finite volume scheme for a simplified hydrostatic model for fluid-structure interaction. *Int J Numer Meth Fluids*. 2022;1-36. doi: 10.1002/fld.5143